ACS APPLIED MATERIALS & INTERFACES

www.acsami.org

Research Article

Photo Energy-Enhanced Oxygen Reduction and Evolution Kinetics in Zn-Air Batteries

Hange Feng, Chaomin Zhang, Menghao Luo, Yuechuan Hu, Zibo Dong, Shaolin Xue,* and Paul K. Chu

Cite This: *ACS Appl. Mater. Interfaces* 2023, 15, 6788−6796

Read Online

ACCESS | Metrics & More | Article Recommendations | Supporting Information

ABSTRACT: Harvesting solar energy directly to boost the sluggish kinetics of oxygen reduction reaction (ORR) and oxygen evolution reaction (OER) on an air cathode is a promising approach. Herein, we synthesize a step-scheme (S-scheme) titanium dioxide-indium selenide (TiO_2-In_2Se_3) heterojunction catalyst. The onset potential in ORR under light illumination reaches 1.28 V and the onset potential decreases to 0.48 V in OER. When an S-scheme TiO_2-In_2Se_3 heterojunction is exposed to light, photogenerated electrons at the conduction band (CB) of TiO_2 migrate to the valence band (VB) of In_2Se_3 due to the built-in electric field. The photogenerated electrons with strong reduction capability on the CB of In_2Se_3 and the holes with strong oxidation capability on the VB of TiO_2 boost the cathode reaction kinetics (ORR/OER). The excellent outcome reveals tremendous commercial potential of photo-enhanced Zn-air batteries.

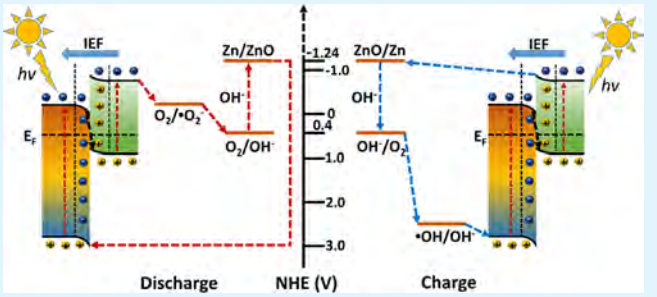

KEYWORDS: *S-scheme heterojunction, photo-introduced, oxygen reduction reaction, oxygen evolution reaction, Zn-air batteries*

INTRODUCTION

Solar energy is a sustainable source of energy[1−3] and can be converted into various forms such as electrical energy.[4−7] So far, numerous studies have been performed on the harvesting of photo energy by semiconductors for photocatalytic degradation of organic pollutants, hydrogen production, CO_2 reduction, and so on.[8−15] In particular, TiO_2 is a good semiconducting photocatalyst due to its chemical stability, low cost, and nontoxicity, and owing to the large bandgap, light absorption by TiO_2 is not efficient. In_2Se_3 also has excellent optical, mechanical, and electrical properties in addition to environmental friendliness.[16−19] In_2Se_3 has a smaller bandgap of 1.36−2.0 eV, and the d^{10} electron configuration of In^{3+} can serve as the main cation in photocatalysis.[20,21] However, poor photoreduction/photooxidation and rapid recombination of photogenerated carriers are drawbacks, and several methods have been proposed to improve the materials.[22−25] In particular, heterojunctions can effectively facilitate the separation and migration of photogenerated carriers during photocatalytic activity, which in turn increases the survival of photogenerated carriers.

The step-scheme (S-scheme) heterojunction proposed by Yu et al. can address the shortcomings and improve the photocatalytic activity.[26−32] An S-scheme heterojunction is typically composed of the reduced photocatalyst (RP) and oxidized photocatalyst (OP). The difference between the work functions of RP and OP allows the free electrons at the interface to migrate until the work functions reach equilibrium, thus producing a built-in electric field (IEF) and band bending at the interface. On one hand, the photogenerated holes of RP and photogenerated electrons of OP in low energy band are recombined under the action of the IEF. On the other hand, photogenerated electrons of PR and holes of OP are retained in high energy band under the effect of energy band bending and contribute to the photocatalytic activity.

Rechargeable Zn-air batteries (ZABs) with a unique semi-open system offer high theoretical density, low cost, high safety, long cycle life, and environmental friendliness, rendering them ideal in energy storage.[33−36] However, they are plagued by the slow oxygen reduction reaction (ORR) and oxygen evolution reaction (OER) kinetics on the air cathodes, H_2 release, and dendrite growth on the Zn anodes, consequently resulting in low discharge and high charge voltages. It has been observed that the discharge voltage is less than 1.2 V and the charge voltage is greater than 2.0 V, which deviates significantly from the equilibrium voltage (1.64 V), resulting in a significant waste of energy.[37−41] Therefore, it is crucial to develop air cathodes with high performance of ORR and OER. TiO_2/C as the cathode proposed by Du et al. exhibits improved OER under light irradiation manifested by smaller charge voltages. The ORR performance of pTTh photo-

Received: October 31, 2022
Accepted: January 13, 2023
Published: January 26, 2023

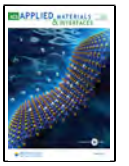

https://doi.org/10.1021/acsami.2c19598
ACS Appl. Mater. Interfaces 2023, 15, 6788−6796

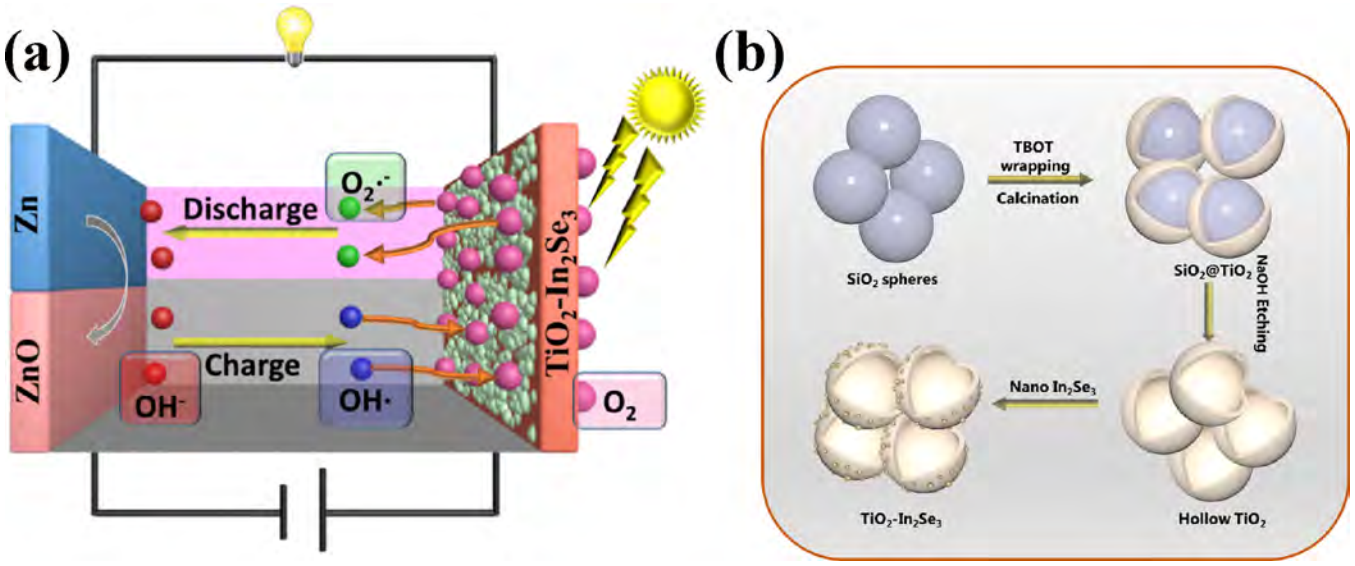

Figure 1. (a) Schematic illustration of the structure of the photo-introduced ZABs and (b) schematic diagram showing the synthesis of TiO_2-In_2Se_3.

electrodes fabricated by Zhou et al. was significantly improved under illumination. In addition, α-Fe_2O_3 and $BiVO_4$ have been used as cathodes to boost the OER performance, and the charging voltage decreases by nearly 0.8 V upon light illumination.[42−44] Single semiconductor photoelectrodes can only promote ORR or OER under illumination.[45−47] The $Ni_{12}P_5$@NCNT p−n junction promotes ORR and OER kinetics during discharging/charging under illumination, resulting in a reduced discharge−charge voltage gap of 0.68 V.[48] Type II $CsPbBr_3$@PCN-333 heterojunction under illumination enables an effective separation of photogenerated carriers, which in turn improves the ORR and OER performance.[49] The S-scheme Fe_2O_3/C_3N_4 heterojunction under illumination allows the strong reductive and oxidative photogenerated carriers to be retained and to facilitate ORR and OER performance.[50]

In this work, an S-scheme TiO_2-In_2Se_3 heterojunction is designed and demonstrated for ZABs. The TiO_2-In_2Se_3 cathode with a large specific surface area (218 m^2 g^{-1}) and porous structure improves the contact area and transport of the reactants. The S-scheme TiO_2-In_2Se_3 heterojunction effectively promotes the separation and migration of photogenerated carriers under illumination, making the electrons and holes more easily retained on the conduction band (CB) of In_2Se_3 and the valence band (VB) of TiO_2. During discharging, electrons on the CB of In_2Se_3 with strong reduction ability reduce O_2 to $\bullet O_2^-$, achieving an onset potential of 1.28 V in ORR. During charging, holes on the VB of TiO_2 with strong oxidation ability oxidize OH^- to •OH, giving rise to an onset potential of 0.48 V in OER. The results reveal an excellent strategy to capture photo energy to enhance the properties of ZABs. Figure 1a shows the schematic structure of the light-introduced ZAB assembly.

EXPERIMENTAL SECTION

Preparation of Hollow TiO_2. Typically, SiO_2 was prepared by a modified Stöber method.[51] The suspension was prepared by dispersing SiO_2 nanoparticles in 30 mL of absolute ethanol, and then 100 mg of hydroxypropyl cellulose (HPC) and 1 mL of deionized water were added and stirred for 0.5 h. Four milliliters of tetrabutyl titanate (TBOT) was added to 11 mL of absolute ethanol and stirred for 10 min, and then the solution was added slowly (1 mL/min) to the above suspension and subsequently transferred to an oil bath to react at 85 °C for 100 min to obtain SiO_2@TiO_2 nanoparticles. The obtained SiO_2@TiO_2 particles were calcined at 550 °C for 2 h. Afterward, SiO_2@TiO_2 were placed in NaOH solution (3 M) and stirred for 6 h to obtain hollow TiO_2 nanoparticles. Finally, the TiO_2 nanoparticles were washed and dried.

Preparation of Hollow TiO_2-In_2Se_3. First, 24 mg of Se powder and 59 mg of $InCl_3$•$4H_2O$ were dissolved in 40 and 10 mL of polyethylene glycol (PEG), respectively, and 1.2 mL of ethylenediamine was added to the former solution and stirred magnetically. The two obtained solutions are mixed, stirred, and heated under argon to 230 °C for 40 min. The solution was then quenched in a water bath to room temperature to obtain a suspension that was washed and dried to obtain the In_2Se_3 nanoparticles. The TiO_2 particles and In_2Se_3 nanoparticles were sonicated and dispersed in 30 and 5 mL of ethanol, respectively, for 2 h. Afterward, two suspensions were placed in an autoclave lined with Teflon and heated to 120 °C for 12 h. The precipitate was washed and dried to obtain TiO_2-In_2Se_3 nanoparticles.

Rechargeable Liquid ZAB Assembly and Testing. The rechargeable ZAB consisted of an air cathode of carbon paper coated with electrocatalyst ink, an anode of a polished zinc plate, and an electrolyte of 6.0 M KOH + 0.2 M $Zn(OAc)_2$. Uniform holes are drilled on both sides of the transparent package of the ZAB to allow the TiO_2-In_2Se_3 catalyst to breathe O_2 and capture photo energy during operation. The ink was prepared by homogeneously mixing 5% solution of Nafion, catalyst powder (loading of 1.0 mg cm^{-2}), and ethanol. Variations of discharge/charge voltages were analyzed at different current densities (0.2 to 10 mA cm^{-2}), and cycle tests were carried out at a current density of 5 mA cm^{-2} for 40 min each (20 min discharging and 20 min charging) while being irradiated with ultraviolet light (365 nm and 90 mW cm^{-2}).

RESULTS AND DISCUSSION

TiO_2-In_2Se_3 is prepared by the typical hard template method, as shown in Figure 1b. This process starts with the synthesis of SiO_2 nanospheres, and the surface morphology of SiO_2 is shown in the Supporting Information (Figure S1). Subsequently, the SiO_2@TiO_2 was fabricated and then the internal SiO_2 was etched to obtain hollow TiO_2. The SEM and TEM images of the hollow TiO_2 are depicted in Figure 2ba,. Finally, TiO_2-In_2Se_3 is synthesized. The main difficulty is that the In_2Se_3 nanoparticles (Figure S2) do not adsorb efficiently on

https://doi.org/10.1021/acsami.2c19598
ACS Appl. Mater. Interfaces 2023, 15, 6788−6796

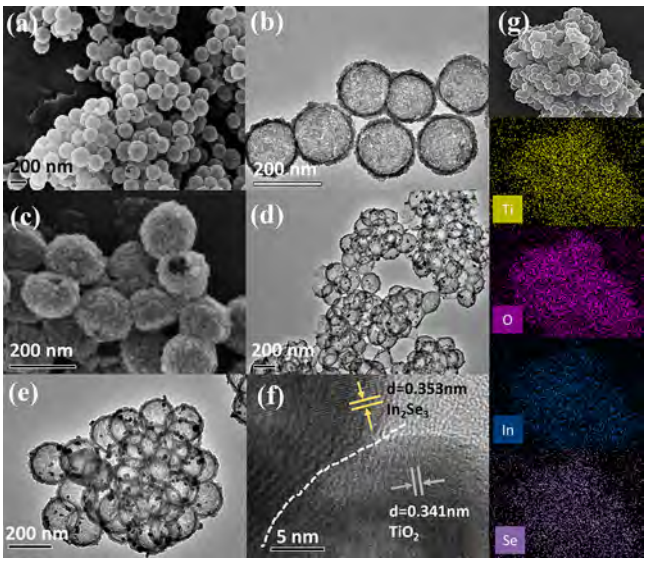

Figure 2. (a) SEM and (b) TEM images of hollow TiO_2; (c) SEM and (d, e) TEM images of hollow TiO_2-In_2Se_3; (f) HR-TEM image of TiO_2-In_2Se_3; (g) elemental maps of TiO_2-In_2Se_3.

the TiO_2 surface due to electrostatic repulsion. Hence, HPC is added to weaken the electrostatic repulsion on TiO_2. Figure 2c–e shows the TEM images of TiO_2-In_2Se_3 and Figure 2f shows the lattice spacing of 0.341 and 0.353 nm, which matches the (101) plane of TiO_2 and the (015) plane of In_2Se_3. The elemental maps in Figure 2g demonstrate successful preparation of the TiO_2-In_2Se_3 composite.

The X-ray diffraction (XRD) spectra of TiO_2, In_2Se_3, and TiO_2-In_2Se_3 are presented in Figure 3a. The peaks at 2θ = 25.3, 37.8, 47.9, 55.1, 62.7, and 70.2° in Figure 3a can be indexed to anatase TiO_2 (JCPDS no. 84-1286), and those at 18.1, 25.3, 28.6, 37.6, 46.4, and 54.3° stem from hexagonal In_2Se_3 (JCPDS no. 23-0294). The characteristic peaks of TiO_2-In_2Se_3 indicate that the crystal structures of TiO_2 and In_2Se_3 are well preserved. The diffraction intensity of TiO_2-In_2Se_3 is weaker than that of pure TiO_2 and In_2Se_3 because of the smaller concentration of TiO_2 and In_2Se_3 in TiO_2-In_2Se_3.

The surface composition and chemical states of TiO_2-In_2Se_3 are characterized by X-ray photoelectron spectroscopy (XPS). Figure S3 shows that the samples are composed of Ti, O, In, and Se. The peak located at 284.6 eV belongs to the C 1s and arises from adventitious hydrocarbons from air exposure. In Figure 3b, the peaks centered at 464.3 and 458.3 eV can be assigned to Ti $2p_{1/2}$ and Ti $2p_{3/2}$, indicating octahedral coordination of Ti^{4+}. The O 1s spectrum in Figure 3c shows the peak at 529.6 eV from the lattice oxygen of Ti-O-Ti and the peak at 531.7 eV from the hydroxyl group of H_2O on the surface.[52,53] Figure 3d shows the XPS pattern of In 3d, and the peaks at 452.2 and 444.8 eV correspond to In $3d_{3/2}$ and In $3d_{5/2}$, respectively, indicating the +3 oxidation state. The Se 3d peak at 54.0 e V indicates that Se is in the form of Se^{2-}, as shown in Figure 3e. Compared to the pristine Ti 2p and O 1s spectra, the binding energy of TiO_2-In_2Se_3 exhibits a small negative shift, meaning a bigger electron density. In contrast, the peaks of In 3d and Se 3d of TiO_2-In_2Se_3 exhibit a small positive shift, implying a smaller electron density. Since the work function of TiO_2 is higher than that of In_2Se_3, free electrons can transfer from In_2Se_3 to TiO_2.[54,55] The results suggest that the strong electron interactions between TiO_2 and In_2Se_3 in the heterostructure promote the redox process of the intermediates.

The specific surface area and porosity of TiO_2, In_2Se_3, and TiO_2-In_2Se_3 are investigated by the N_2 adsorption–desorption method. The N_2 adsorption–desorption isothermal curves in Figure 3f and Figure S4 show that the TiO_2 and TiO_2-In_2Se_3 isotherms belong to type IV with well-defined hysteresis loops, indicating that both have the mesoporous structure. Figure 3f reveals that the catalyst exhibits infinite adsorption of N_2 around P/P_0 = 1, indicating the presence of large mesopores in the catalyst. The specific surface areas of TiO_2 and TiO_2-In_2Se_3 are 187 and 218 $m^2\ g^{-1}$ depending on the Brunauer–Emmett–Teller (BET) isotherm. Figure S4 shows the Barrett–Joyner–Halenda (BJH) pore size distributions and that of TiO_2-In_2Se_3 is ~6 nm, suggesting the typical hollow mesoporous structure.

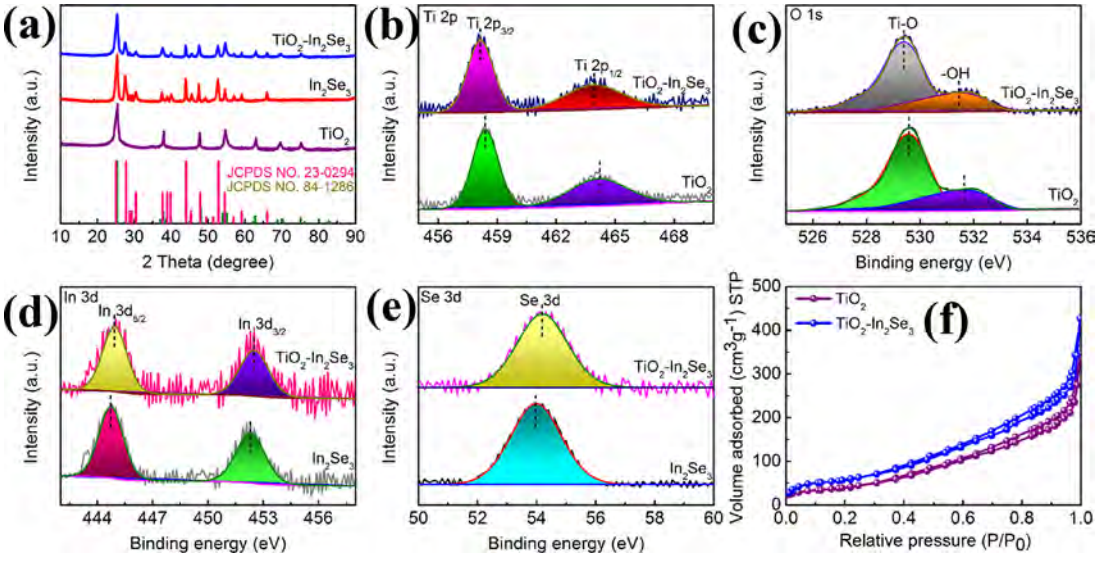

Figure 3. (a) XRD patterns of TiO_2, In_2Se_3, and TiO_2-In_2Se_3; XPS spectra of TiO_2-In_2Se_3: (b) Ti 2p, (c) O 1s, (d) In 3d, and (e) Se 3d; (f) nitrogen adsorption–desorption isotherms of TiO_2 and TiO_2-In_2Se_3.

https://doi.org/10.1021/acsami.2c19598
ACS Appl. Mater. Interfaces 2023, 15, 6788–6796

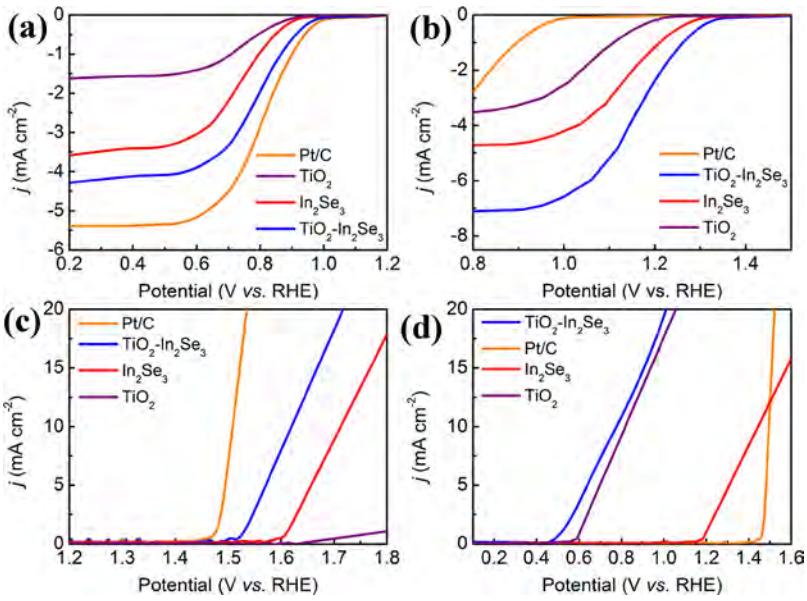

Figure 4. ORR polarization curves of Pt/C, TiO_2, In_2Se_3, and TiO_2-In_2Se_3 at a scan rate of 5 mV s^{-1}: (a) without light illumination and (b) with light illumination. OER polarization curves of Pt/C, TiO_2, In_2Se_3, and TiO_2-In_2Se_3: (c) without light illumination and (d) with light irradiation.

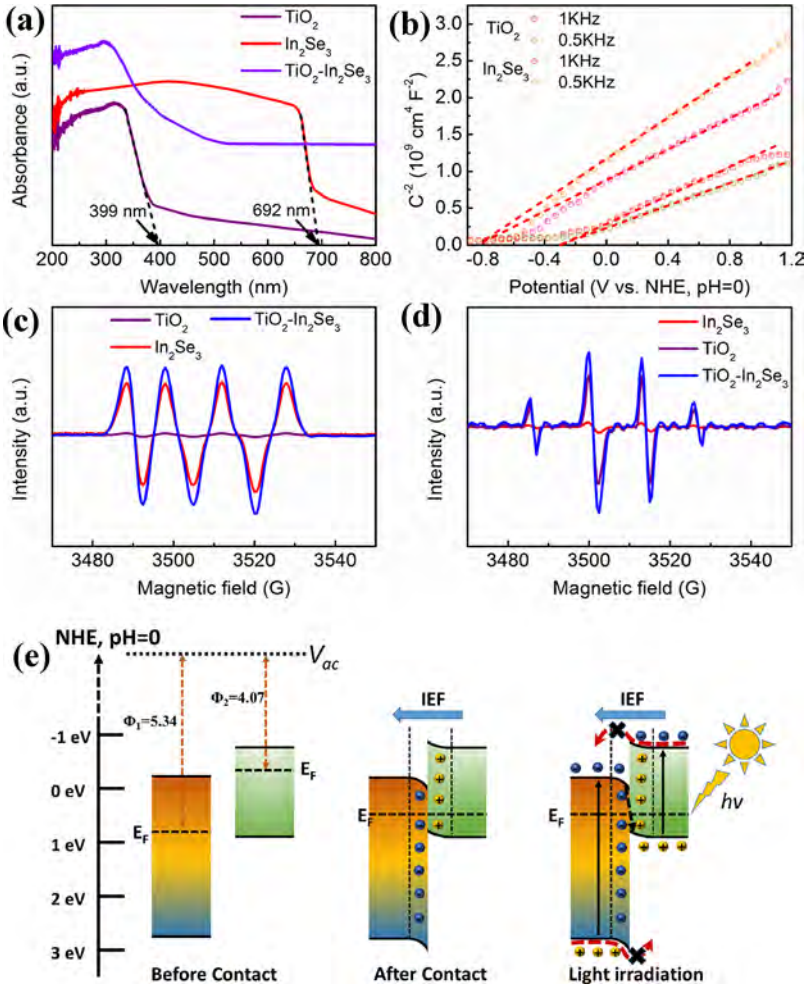

Figure 5. (a) UV−vis spectra of TiO_2, In_2Se_3, and TiO_2-In_2Se_3; (b) M-S plots of TiO_2 and In_2Se_3 at 0.5 and 1.0 kHz; EPR spectra of (c) DMPO-•O_2^- and (d) DMPO-•OH of TiO_2, In_2Se_3, and TiO_2-In_2Se_3 upon light illumination; (e) schematic diagram of TiO_2 and In_2Se_3 before/after contact and the creation of band bending and IEF.

https://doi.org/10.1021/acsami.2c19598
ACS Appl. Mater. Interfaces 2023, 15, 6788−6796

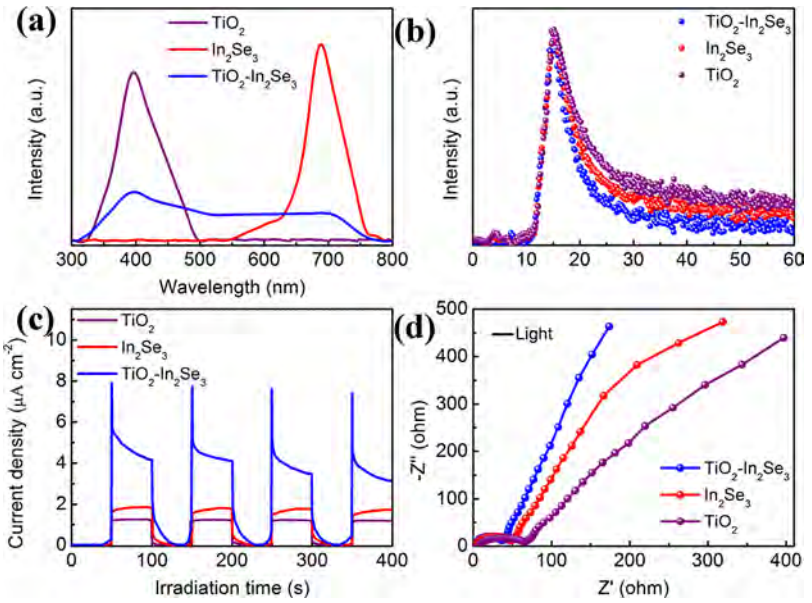

Figure 6. (a) PL spectra, (b) time-resolved PL spectra, (c) transient photocurrent response, and (d) EIS curves of TiO_2, In_2Se_3, and TiO_2-In_2Se_3.

In this work, the ORR and OER activities of TiO_2, In_2Se_3, TiO_2-In_2Se_3, and Pt/C are investigated using a three-electrode system in which the electrolyte is 0.1 M KOH saturated with O_2. The linear scanning voltammetry curves of the catalysts under dark and illumination at a scan rate of 5 mV s^{-1} are shown in Figure 4a,b. It is observed that the onset potential (the potential at which the current reaches 0.1 mA cm^{-2}) of the catalyst under illumination is higher than in the dark. In particular, in the ORR of TiO_2-In_2Se_3, an onset potential of 1.28 V (*vs* normal hydrogen electrode (NHE)) is observed under illumination, which is 0.32 V higher than in the dark (0.96 V) and also higher than the onset potential of Pt/C (0.99 V). The ORR kinetics is further studied by the Tafel curves. Figure S5a,b shows that the slopes of the catalysts under illumination are larger, and so the ORR kinetics is better during light exposure. Figure 4c,d shows the OER curves of TiO_2, In_2Se_3, TiO_2-In_2Se_3, and Pt/C without and with light. The OER onset potential of TiO_2-In_2Se_3 under illumination (0.48 V) is lower than without illumination and also lower than the onset potential of Pt/C (1.47 V). Meanwhile, the OER onset potential of all catalysts is lower upon light exposure. The Tafel curves in Figure S5c,d illustrate that the OER kinetics is better in the presence of light. Subsequently, the ORR and OER activities of TiO_2-In_2Se_3 are monitored for up to 5 h, and as shown in Figure S6, the potentials are stable and unaffected by light irradiation.

The optical absorption properties of TiO_2, In_2Se_3, and TiO_2-In_2Se_3 are determined by ultraviolet−visible diffuse reflectance spectroscopy (UV−vis DRS), as shown in Figure 5a. The absorption band edges of pure TiO_2 and In_2Se_3 are 399 and 692 nm, respectively. The bandgap (E_g) of a semiconductor is calculated by the following empirical formula: $E_g = 1240/\lambda$, where λ is the absorption band edge and the bandgaps of TiO_2 and In_2Se_3 are 3.10 and 1.79 eV, respectively. Light absorption by pristine TiO_2 is relatively narrow, mainly in the UV region. However, when TiO_2 and In_2Se_3 are combined, light absorption of TiO_2-In_2Se_3 extends to the visible region due to strong light absorption by In_2Se_3 at $\lambda > 550$ nm. To investigate the band structure of TiO_2 and In_2Se_3, the Mott−Schottky (M-S) curves at 0.5 and 1.0 kHz were analyzed (Figure 5b). The slopes of the M-S curves are both positive, indicating that both TiO_2 and In_2Se_3 are *n*-type semiconductors, and their flat-band potentials (E_{fb}) (*vs* NHE, pH = 0) are −0.29 and −0.84 V, respectively. According to previous findings, the E_{fb} of an *n*-type semiconductor is approximately at the same position as the CB potential.[56−59] The CB potentials of TiO_2 and In_2Se_3 are −0.29 and −0.84 eV, respectively, and based on E_g calculated by UV−vis DRS, the CB potentials of TiO_2 and In_2Se_3 are 2.81 and 0.95 eV, respectively. The schematic band structures of TiO_2 and In_2Se_3 are depicted in Figure S7.

The different work functions (Φ) of semiconductors provide the driving force for the transfer of free charge at the interface. Φ of TiO_2 and In_2Se_3 is determined by ultraviolet photoelectron spectroscopy (UPS) (Figure S8). The UPS is measured at infinite close to vacuum and bias pressure. The work function of a semiconductor is calculated by the following equation: $\Phi = h\nu - |E_{cutoff} - E_F|$, where $h\nu$ is defined as the energy of the excited photon in the test (21.22 eV), E_{cutoff} represents the cutoff energy, and E_F represents the Fermi energy level. The UPS curves show the E_{cutoff} of 15.88 and 17.25 eV for TiO_2 and In_2Se_3 when the E_F is 0 eV. The calculated Φ for TiO_2 and In_2Se_3 are 5.34 and 4.07 eV, respectively.

The short-lived oxygen-containing intermediates are trapped during light illumination by dimethylpyridine N-oxide (DMPO) and detected by electron paramagnetic resonance (EPR) spin trapping. The transfer mechanism at the interface of the photogenerated carriers is verified by the characteristic peaks of the intermediates. The redox potentials of the O_2/$\bullet O_2^-$, H_2O/$\bullet$OH, and OH^-/$\bullet$OH couples are −0.33, 2.37, and 2.69 eV, respectively (Figure S7).[26,28,29] Figure 5c,d shows the EPR peaks of DMPO-$\bullet O_2^-$ and DMPO-$\bullet$OH for TiO_2, In_2Se_3, and TiO_2-In_2Se_3. There is no EPR peak of DMPO-$\bullet O_2^-$ from TiO_2 as the CB potential of TiO_2 is more positive than the redox potential of the O_2/$\bullet O_2^-$ couple. Figure 5c shows the EPR peaks of DMPO-$\bullet$OH of TiO_2 and TiO_2-In_2Se_3. No EPR peak of DMPO-$\bullet$OH appears from In_2Se_3 because the VB potential of In_2Se_3 is more negative than the redox potential of the OH^-/$\bullet$OH couple. Furthermore, the

https://doi.org/10.1021/acsami.2c19598
ACS Appl. Mater. Interfaces 2023, 15, 6788−6796

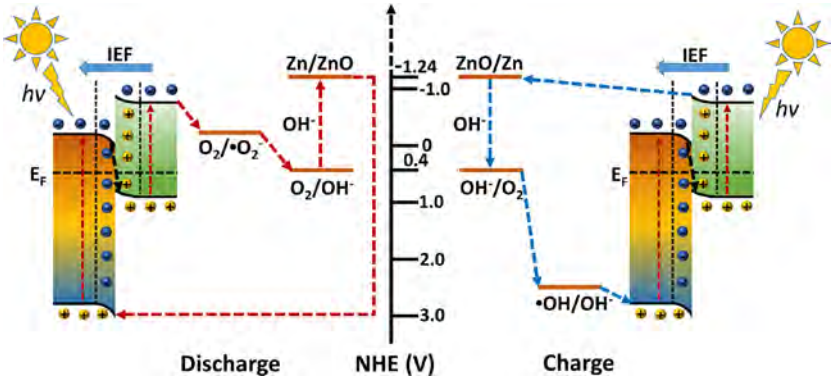

Figure 7. Schematic illustration of the discharge and charge working mechanism on the S-scheme TiO_2-In_2Se_3 heterojunction under illumination.

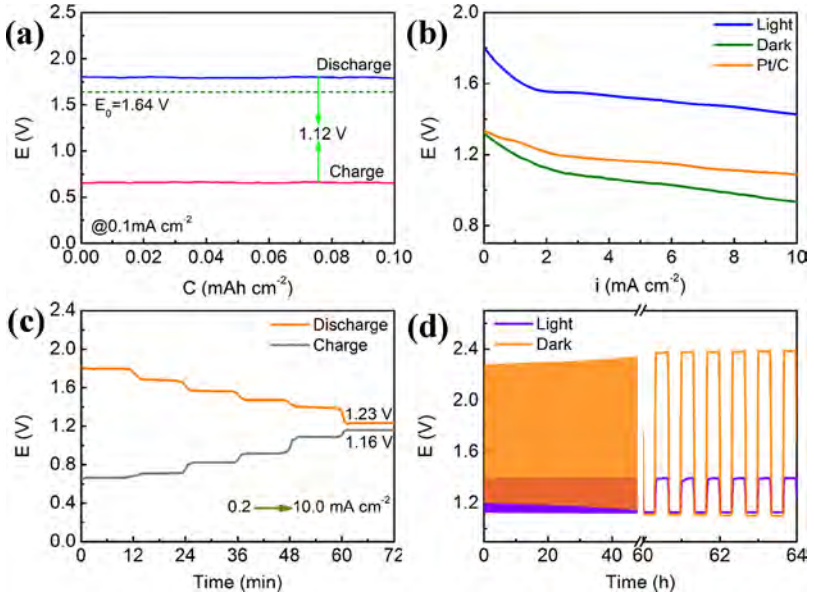

Figure 8. (a) Discharge/charge curves of the TiO_2-In_2Se_3-based ZAB under illumination at 0.1 mA cm^{-2}; (b) discharge curves of the Pt/C-based and TiO_2-In_2Se_3-based Pt/C-based ZAB under dark and illumination at a sweep rate of 0.01 mA s^{-1}; (c) variation of discharge voltage at different current densities under illumination; (d) discharge−charge cycling of the ZAB at 5.0 mA cm^{-2}.

intensity of the EPR peak of DMPO-•O_2^- follows the order In_2Se_3 < TiO_2-In_2Se_3, and that of DMPO-•OH shows the trend TiO_2 < TiO_2-In_2Se_3. If the charge transfer mechanism of the TiO_2-In_2Se_3 heterojunction is the conventional type II, it should not promote the production of •O_2^- and •OH radicals (Figure 5d). However, the EPR spectra of DMPO-•O_2^- and DMPO-•OH for TiO_2, In_2Se_3, and TiO_2-In_2Se_3 reveal that the signal intensity of TiO_2-In_2Se_3 is higher than that of pristine TiO_2 and In_2Se_3. As a consequence, the photogenerated charge transfer in TiO_2-In_2Se_3 follows the S-scheme mechanism (Figure 5e).

The transfer kinetics of photogenerated carriers is studied by photoluminescence (PL), time-resolved photoluminescence (TRPL), as well as photo-electrochemistry properties of the catalyst. Recombination of photogenerated carriers on TiO_2-In_2Se_3 under monochromatic light excitation is analyzed by PL (Figure 6a). The pristine TiO_2 and In_2Se_3 exhibit intense fluorescence under excitation by monochromatic light (λ = 300 nm), indicating that a large number of photogenerated electrons and holes recombine. The fluorescence intensity of TiO_2-In_2Se_3 decreases when In_2Se_3 is deposited on TiO_2, reflecting that the heterojunction formed at the interface between TiO_2 and In_2Se_3 allows charge recombination to be alleviated.

Migration of photogenerated carriers at the interface of the TiO_2-In_2Se_3 heterojunction is verified by TRPL (Figure 6b). The average decay time (τ_a) of photogenerated carriers is calculated from the formula $\tau_a = (A_1\tau_1^2 + A_2\tau_2^2)/(A_1\tau_1 + A_2\tau_2)$,[60] where τ_1 and τ_2 represent the short lifetime of the radiative pathway of photogenerated carriers and long lifetime of the non-radiative pathway, respectively, and and A_1 and A_2 denote the pre-exponential coefficients of the decay curves. The specific values of τ_1, τ_2, A_1, and A_2 are shown in Table S1. The calculated τ_a values of TiO_2, In_2Se_3, and TiO_2-In_2Se_3 are 3.97, 3.69, and 2.91 ns, respectively, and the radiative and non-radiative lifetimes of TiO_2-In_2Se_3 are lower than those of the pristine TiO_2 and In_2Se_3, revealing efficient migration of photogenerated carriers at the S-scheme TiO_2-In_2Se_3 heterojunction.

The separation and transfer efficiency of the photogenerated carriers is analyzed by investigating the photochemical properties of the catalyst. As shown in Figure 6c, the photocurrents of TiO_2, In_2Se_3, and TiO_2-In_2Se_3 increase rapidly when the light source is turned on and decrease rapidly in reverse. At the same time, the photocurrent of TiO_2-

https://doi.org/10.1021/acsami.2c19598
ACS Appl. Mater. Interfaces 2023, 15, 6788−6796

In_2Se_3 is greater than those of the pristine TiO_2 and In_2Se_3. Therefore, the S-scheme heterojunction facilitates migration and separation of photogenerated electrons and holes. According to the Nyquist curves with light exposure (Figure 6d) and without light irradiation (Figure S9), the radius of the TiO_2-In_2Se_3 curve is smaller than those of the single TiO_2 and In_2Se_3. The S-scheme heterojunction reduces the resistance against movement of photogenerated carriers. The interfacial charge transfer resistance is larger in the dark, suggesting that the carriers on TiO_2-In_2Se_3 are separated under light illumination and hence electrons and holes are transferred efficiently to the O_2/OH^- redox pairs in ORR and OER.

Figure 7 illustrates the mechanism of OER and ORR during light exposure. The transfer of photogenerated carriers at the interface of the TiO_2-In_2Se_3 photoelectrode under illumination follows the S-scheme. Photogenerated electrons on the CB of TiO_2 migrate to the VB of In_2Se_3 under the effect of IEF. During discharging, since the CB potential of In_2Se_3 (−0.84 V) is more negative than $O_2/{\bullet}O_2^-$ (−0.33 V), the electrons retained on the CB of In_2Se_3 reduce the O_2 to ${\bullet}O_2^-$ on the catalyst surface, which in turn reduce ${\bullet}O_2^-$ to OH^-. In this process, the theoretical discharge voltage is equal to the potential difference between the VB of TiO_2 and Zn/ZnO, which is higher than the equilibrium voltage of ZABs in the dark (1.64 V). During charging, it is evident from the above results that the holes retained on the VB of TiO_2 oxidize OH^- to ${\bullet}OH$, thereby decomposing to produce O_2. Similarly, the theoretical value of the charge voltage is equal to the potential difference between the CB of In_2Se_3 and Zn/ZnO.

Figure 8a shows the discharge/charge properties of the TiO_2-In_2Se_3-based ZAB under illumination at a current density of 0.1 mA cm^{-2}. The discharge voltage of the TiO_2-In_2Se_3-based ZAB (1.79 V) is 510 and 150 mV higher than the Pt/C-based ZAB (1.28 V) in Figure S10 and the theoretical values of the ZAB (1.64 V) in the dark, respectively. And the charge voltage is as low as 0.67 V, which contrasts with the Pt/C-based ZAB (1.82 V). These excellent results are attributed to the effect of S-scheme heterojunctions, whereby photogenerated carriers are more readily preserved on the CB of In_2Se_3 and the VB of TiO_2, promoting ORR and OER and allowing the conversion of photo energy to electrical energy. Figure 8b shows the discharge curves for TiO_2-In_2Se_3-based and Pt/C-based ZABs under dark and illumination at a scan rate of 0.01 mA s^{-1}. At less than 8.0 mA cm^{-2}, the discharging voltage of the TiO_2-In_2Se_3-based ZAB upon light irradiation is significantly higher than that in the dark and also higher than that of the Pt/C-based ZAB. The properties are superior to ZABs with and without light exposure, as shown in Table S2. Even at AM1.5, the discharge voltage is higher than the charge voltage at current densities less than 0.5 mA cm^{-2}, as shown in Figure S11.

The variation of the discharge/charge voltage of the ZAB at different current densities under the same light exposure is shown in Figure 8. With the current density gradually increasing from 0.2 to 10 mA cm^{-2}, the discharge voltage decreases from 1.79 to 1.23 V and the charge voltage increases from 0.67 to 1.16 V. And the discharge voltage is always higher than the charge voltage during this process. This superior performance under illumination contrasts with the ZAB under dark conditions in Figure S12. The cycling stability with and without light illumination at a current density of 5 mA cm^{-2} is shown in Figure 8d. The discharge and charge voltages of the TiO_2-In_2Se_3-based ZAB are stable at 1.39 and 1.12 V under illumination, respectively, and the discharge voltage is higher than that of the Pt/C-based ZAB in the dark (Figure S13), as well as the charge voltage is lower than it. The excellent cycling stability of the catalyst is further demonstrated by XRD, SEM, and TEM, as shown in Figures S14 and S15a,b. The incident photon−current efficiencies (IPCE) of ZABs at different current densities are shown in Figure S16a,b. With increasing current density, the value of IPCE gradually increases, indicating a gradual increase in the contribution of photo energy. However, the contribution of photo energy will diminish as the current increases sharply; this is mainly attributed to the lifetime of the photogenerated carriers in the cathode not being sufficient for the multi-electron transfer process of the ORR/OER. For future work, it is believed that the selection of suitable semiconductor materials, microstructure adjustment of semiconductors, and introduction of external fields are believed to enable the semiconductor electrodes to have a large active surface, wide light absorption range, and strong photogenerated carrier separation capability; this can significantly increase the power density and IPCE of light-introduced ZABs.

CONCLUSIONS

An S-scheme TiO_2-In_2Se_3 heterojunction with a large specific surface area (218 m^2 g^{-1}) is designed and demonstrated. Owing to the different work functions between TiO_2 and In_2Se_3, free electrons are transferred from the side with a low work function to that with a high work function to form an IEF at the interface, which drives the flow of photogenerated electrons from the CB of TiO_2 to the VB of In_2Se_3. The photogenerated electrons at the CB of In_2Se_3 with the strong reducing capacity promote ORR and raise the onset potential to 1.28 V, which in turn increases the output voltage. The photogenerated holes at the VB of TiO_2 with the strong oxidation capacity promote OER and reduce the onset potential to 0.48 V. Therefore, the photoelectrode converts photo energy into electrical energy, and the ZAB achieves a discharge voltage of 1.79 V and a charge voltage of 0.67 V. The results reveal a new strategy to improve the performance of ZABs.

ASSOCIATED CONTENT

Supporting Information

The Supporting Information is available free of charge at https://pubs.acs.org/doi/10.1021/acsami.2c19598.

Materials characterization, electrochemical characterization, SEM and TEM images, XPS spectrum, pore size distribution curves, XPS spectrum, ORR and OER Tafel plots, polarization curves, band structures, UPS plots, EIS curves of different materials, discharging and charging curves, XRD spectra of TiO_2-In_2Se_3, and discharge−charge cycling curves of Pt/C (PDF)

AUTHOR INFORMATION

Corresponding Author

Shaolin Xue − *College of Science, Donghua University, Shanghai 201620, P.R. China; Shanghai Institute of Intelligent Electronics and Systems, Donghua University, Shanghai 201620, China;* orcid.org/0000-0001-5876-7886; Email: slxue@dhu.edu.cn; Fax: +86 21 67792089

https://doi.org/10.1021/acsami.2c19598
ACS Appl. Mater. Interfaces 2023, 15, 6788−6796

Authors

Hange Feng − *College of Information Science and Technology and College of Science, Donghua University, Shanghai 201620, P.R. China*

Chaomin Zhang − *School of Mathematics, Physics and Statistics, Shanghai University of Engineering Science, Shanghai 201620, China*

Menghao Luo − *College of Science, Donghua University, Shanghai 201620, P.R. China*

Yuechuan Hu − *College of Science, Donghua University, Shanghai 201620, P.R. China*

Zibo Dong − *College of Science, Donghua University, Shanghai 201620, P.R. China*

Paul K. Chu − *Department of Physics, Department of Materials Science and Engineering, and Department of Biomedical Engineering, City University of Hong Kong, Kowloon 999077, Hong Kong, China;* orcid.org/0000-0002-5581-4883

Complete contact information is available at: https://pubs.acs.org/10.1021/acsami.2c19598

Author Contributions

All author contributions in the manuscript are equal. All authors approved the final version of the manuscript.

Notes

The authors declare no competing financial interest.

■ ACKNOWLEDGMENTS

The work was supported by the Fundamental Research Funds for the Central Universities and Graduate Student Innovation Fund of Donghua University (CUSF-DH-D-2021049), City University of Hong Kong Donation Research Grant (DON-RMG 9229021), City University of Hong Kong Donation Grant (9220061), and City University of Hong Kong Strategic Research Grant (SRG) (no. 7005505).

■ REFERENCES

(1) Polman, A.; Knight, M.; Garnett, E.; Ehrler, B.; Sinke, W. Photovoltaic Materials: Present Efficiencies and Future Challenges. *Science* **2016**, *352*, 4424−4424.

(2) Li, F.; Chen, J. Mechanistic Evolution of Aprotic Lithium-Oxygen Batteries. *Adv. Energy Mater.* **2017**, *7*, 1602934.

(3) Todorov, T. K.; Reuter, K. B.; Mitzi, D. B. High-Efficiency Solar Cell with Earth-Abundant Liquid-Processed Absorber. *Adv. Mater.* **2010**, *22*, 156−159.

(4) Cariou, R.; Benick, J.; Feldmann, F.; Hohn, O.; Hauser, H.; Beutel, P.; Razek, N.; Wimplinger, M.; Blasi, B.; Lackner, D.; Hermle, M.; Siefer, G.; Glunz, S. W.; Bett, A. W.; Dimroth, F. III-V-on-Silicon solar Cells Reaching 33% Photoconversion Efficiency in Two-Terminal Configuration. *Nat. Energy* **2018**, *3*, 326−333.

(5) Kunzmann; Valero, S.; Sepúlveda, Á.; Santacruz, M.; Lalinde, E.; Berenguer, J.; Martínez, J.; Guldi, D.; Serrano, E.; Costa, R. Hybrid Dye-Titania Nanoparticles for Superior Low-Temperature Dye-Sensitized Solar Cells. *Adv. Energy Mater.* **2018**, *8*, 1702583.

(6) Huang, J.; Lai, M.; Lin, J.; Yang, P. Rich Chemistry in Inorganic Halide Perovskite Nanostructures. *Adv. Mater.* **2018**, *30*, 1802856.

(7) Ahmad, S.; George, C.; Beesley, D.; Baumberg, J.; Volder, M. Photo-Rechargeable Organo-Halide Perovskite Batteries. *Chem. Soc. Rev.* **2020**, *49*, 1414−1448.

(8) Kumaravel, V.; Mathew, S.; Bartlett, J.; Pillai, S. C. Photocatalytic Hydrogen Production Using Metal Doped TiO_2: A Review of Recent Advances. *Appl. Catal. B* **2018**, *244*, 1021−1064.

(9) Zangeneh, H.; Zinatizadeh, A.; Habibi, M.; Akia, M.; Isa, M. H. Photocatalytic Oxidation of Organic Dyes and Pollutants in Wastewater Using Different Modified Titanium Dioxides: A Comparative Review. *J. Ind. Eng. Chem.* **2015**, *26*, 1−36.

(10) Ma, R.; Zhang, S.; Wen, T.; Gu, P.; Li, L.; Zhao, G.; Niu, F. L.; Huang, Q. F.; Tang, Z. W.; Wang, X. K. A Critical Review on Visible-Light-Response CeO_2-Bbased Photocatalysts with Enhanced Photooxidation of Organic Pollutants. *Catal. Today* **2018**, *335*, 20−30.

(11) Pirhashemi, M.; Habibi-Yangjeh, A. Ultrasonic-Assisted Preparation of Plasmonic ZnO/Ag/Ag_2WO_4 Nanocomposites with High Visible-Light Photocatalytic Performance for Degradation of Organic Pollutants. *J. Colloid. Interface Sci.* **2017**, *491*, 216−229.

(12) Wang, S.; Zhu, B.; Liu, M.; Zhang, L.; Yu, J.; Zhou, M. Direct Z-Scheme Zno/Cds Hierarchical Photocatalyst for Enhanced Photocatalytic H_2-Production Activity. *Appl. Catal. B Environ.* **2019**, *243*, 19−26.

(13) Meng, A.; Zhu, B.; Zhong, B.; Zhang, L.; Cheng, B. Direct Z-Scheme TiO_2/CDs Hierarchical Photocatalyst for Enhanced Photocatalytic H_2 Production Activity. *Appl. Surf. Sci.* **2017**, *422*, 518−527.

(14) Gao, C.; Meng, Q.; Zhao, K.; Yin, H.; Wang, D.; Guo, J.; Zhao, S.; Chang, L.; He, M.; Li, Q.; Zhao, H.; Huang, X.; Gao, Y.; Tang, Z. Co_3O_4 Hexagonal Platelets with Controllable Facets Enabling Highly Efficient Visible-Light Photocatalytic Reduction of CO_2. *Adv. Mater.* **2016**, *28*, 6485.

(15) Wu, Y. A.; Mcnulty, I.; Liu, C.; Lau, K. C.; Rajh, T. Author Correction: Facet-Dependent Active Sites of a Single Cu_2O Particle Photocatalyst for CO_2 Reduction to Methanol. *Nat. Energy* **2019**, *4*, 1−12.

(16) Wang, R.; Wan, J.; Jia, J.; Xue, W.; Hu, X.; Liu, E.; Fan, J. Synthesis of In_2Se_3 Homojunction Photocatalyst with α and γ Phases for Efficient Photocatalytic Performance. *Mater. Design* **2018**, *151*, 74−82.

(17) Island, J. O.; Blanter, S. I.; Buscema, M.; van der Zant, H. S.; Castellanos-Gomez, A. Gate Controlled Photocurrent Generation Mechanisms in High-Gain In(2)Se(3) Phototransistors. *Nano Lett.* **2015**, *15*, 7853−7858.

(18) Li, Z.; Ma, H.; Zang, L.; Li, D.; Guo, S.; Shi, L. Construction of Nano-Flower MIL-125(Mo)-In_2Se_3 Z-Scheme Heterojunctions by One-Step Solvothermal Method for Removal of Tetracycline From Wastewater in the Synergy of Adsorption and Photocatalysis Way. *Sep. Purif. Technol.* **2021**, *276*, 119355.

(19) Jiang, Y.; Wang, Q.; Han, L.; Zhang, X.; Jiang, L.; Wu, Z.; Lai, Y.; Wang, D.; Liu, F. Construction of In_2Se_3/MoS_2 Heterojunction as Photoanode toward Efficient Photoelectrochemical Water Splitting. *Chem. Eng. J.* **2019**, *358*, 752−758.

(20) Fu, X.; Wang, X.; Chen, Z.; Zhang, Z.; Li, Z.; Leung, D. Y. C.; Wu, L.; Fu, X. Photocatalytic Performance of Tetragonal and Cubic β-In_2S_3 for the Water Splitting Under Visible Light Irradiation. *Appl. Catal. B Environ.* **2010**, *95*, 393−399.

(21) Wei, X.; Feng, H.; Li, L.; Gong, J.; Jiang, K.; Xue, S.; Chu, P. K. Synthesis of Tetragonal Prismatic γ-In_2Se_3 Nanostructures with Predominantly {110} Facets and Photocatalytic Degradation of Tetracycline. *Appl. Catal. B Environ* **2020**, *260*, 118218.

(22) Mamaghani, A.; Haghighat, F.; Lee, C. Photocatalytic Oxidation Technology for Indoor Environment Air Purification: The State-of-the-Art. *Appl. Catal. B* **2020**, *269*, 118735.

(23) Tang, H.; Ren, Y.; Wei, S.; Liu, G.; Xu, X. Preparation of 3D Ordered Mesoporous Anatase TiO_2 and Their Photocatalytic Activity. *Rare Met.* **2019**, *38*, 453−458.

(24) Xu, C.; Anusuyadevi, P.; Aymonier, C.; Luque, R.; Marre, S. Nanostructured Materials for Photocatalysis. *Chem. Soc. Rev.* **2019**, *48*, 3868−3902.

(25) Wang, L.; Zhu, B.; Cheng, B.; Zhang, J.; Zhang, L.; Yu, J. *In-situ* Preparation of TiO_2/N-Doped Graphene Hollow Sphere Photocatalyst with Enhanced Photocatalytic CO_2 Reduction Performance. *Chin. J. Catal.* **2021**, *42*, 1648−1658.

(26) Xu, Q.; Zhang, L.; Cheng, B.; Fan, J.; Yu, J. S-Scheme Heterojunction Photocatalyst. *Chem* **2020**, *6*, 1543.

(27) Cheng, C.; He, B.; Fan, J.; Cheng, B.; Cao, S.; Yu, J. An Inorganic/Organic S-Scheme Heterojunction H_2-Production Photo-

catalyst and Its Charge Transfer Mechanism. *Adv. Mater.* **2021**, *33*, 2100317.
(28) Xia, P.; Cao, S.; Zhu, B.; Liu, M.; Shi, M.; Yu, J.; Zhang, Y. Designing a 0D/2D S-Scheme Heterojunction Over Polymeric Carbon Nitride for Visible-Light Photocatalytic Inactivation of Bacteria. *Angew. Chem., Int. Ed.* **2020**, *59*, 5218.
(29) Wang, Z.; Chen, Y.; Zhang, L.; Cheng, B.; Yu, J.; Fan, J. Step-Scheme CdS/TiO_2 Nanocomposite Hollow Microsphere with Enhanced Photocatalytic CO_2 Reduction Activity. *J. Mater. Sci. Technol.* **2020**, *56*, 143.
(30) Zhang, L.; Zhang, J.; Yu, H.; Yu, J. Emerging S-Scheme Photocatalyst. *Adv. Mater.* **2022**, *34*, 2107668.
(31) Xu, F.; Meng, K.; Cheng, B.; Wang, S.; Xu, J.; Yu, J. Unique S-Scheme Heterojunctions in Self-Assembled $TiO_2/CsPbBr_3$ Hybrids for CO_2 Photoreduction. *Nat. Commun.* **2020**, *11*, 4613.
(32) Wang, J.; Wang, G.; Cheng, B.; Yu, J.; Fan, J. Sulfur-Doped g-C_3N_4/TiO_2 S-Scheme Heterojunction Photocatalyst for Congo Red Photodegradation. *Chin. J. Catal.* **2021**, *42*, 56−68.
(33) Li, B.; Zhang, S.; Wang, B.; Xia, Z.; Tang, C.; Zhang, Q. A Porphyrin Covalent Organic Framework Cathode for Flexible Zn-Air Batteries. *Energy Environ. Sci.* **2018**, *11*, 1723−1729.
(34) Yang, L.; Zhang, X.; Yu, L.; Hou, J.; Zhou, Z.; Lv, R. Atomic Fe-N_4/C in Flexible Carbon Fiber Membrane as Binder-Free Air Cathode for Zn-air Batteries with Stable Cycling Over 1000 h. *Adv. Mater.* **2022**, *34*, 2105410.
(35) Wei, T.; Li, Q.; Yang, G.; Wang, C. Pseudo-Zn-Air and Zn-Ion Intercalation Dual Mechanisms to Realize High-Areal Capacitance and Long-Life Energy Storage in Aqueous Zn-Battery. *Adv. Energy Mater.* **2019**, *9*, 1901480.
(36) Liu, W.; Yu, L.; Yin, R.; Xu, X.; Feng, J.; Jiang, X.; Zheng, D.; Gao, X.; Que, W. Non-3D Metal Modulation of a 2D Ni-Co Heterostructure Array as Multifunctional Electrocatalyst for Portable Overall Water Splitting. *Small* **2020**, *16*, 1906775.
(37) Lee, J.; Kim, S.; Cao, R.; Choi, N.; Liu, M.; Lee, K.; Cho, J. Metal-Air Batteries with High Energy Density: Li-Air versus Zn-air. *Adv. Energy Mater.* **2011**, *1*, 34−50.
(38) Zhao, Q.; Yan, Z.; Chen, C.; Chen, J. Controlled Preparation, Oxygen Reduction/Evolution Reaction Application, and Beyond. *Chem. Rev.* **2017**, *117*, 10121.
(39) Zhao, Z.; Fan, X.; Ding, J.; Hu, W.; Zhong, C.; Lu, J. Challenges in Zinc Electrodes for Alkaline Zinc-Air Batteries: Obstacles to Commercialization. *ACS Energy Lett.* **2019**, *4*, 2259−2270.
(40) Li, C.; Han, X.; Cheng, F.; Hu, Y.; Chen, C.; Chen, J. Phase and Composition Controllable Synthesis of Cobalt Manganese Spinel Nanoparticles towards Efficient Oxygen Electrocatalysis. *Nat. Commun.* **2015**, *6*, 7345.
(41) Han, X.; He, G.; He, Y.; Zhang, J.; Zheng, X.; Li, L.; Zhong, C.; Hu, W.; Deng, Y.; Ma, T. Engineering Catalytic Active Sites on Cobalt Oxide Surface for Enhanced Oxygen Electrocatalysis. *Adv. Energy Mater.* **2018**, *8*, 1702222.1−1702222.13.
(42) Du, D.; Zhao, S.; Zhu, Z.; Li, F.; Chen, J. Photo-Excited Oxygen Reduction and Oxygen Evolution Reactions Enabling a High-Performance Zn-Air Battery. *Angew. Chem., Int. Ed.* **2020**, *59*, 18140−18144.
(43) Liu, W.; Yang, Y.; Hu, X.; Zhang, Q.; Wang, C.; Wei, J.; Xie, Z.; Zhou, Z. Light-Assisted Li-O_2 Batteries with Lowered Bias Voltages by Redox Mediators. *Small* **2022**, *18*, 2200334.
(44) Liu, X.; Yuan, Y.; Liu, J.; Liu, B.; Chen, X.; Ding, J.; Han, X.; Deng, Y.; Zhong, C.; Hu, W. Utilizing Solar Energy to Improve the Oxygen Evolution Reaction Kinetics in Zinc-Air Battery. *Nat. Commun.* **2019**, *10*, 1−10.
(45) Fang, Z.; Zhang, Y.; Hu, X.; Fu, X.; Dai, L.; Yu, D. Tactile UV- and Solar-Light Multi-Sensing Rechargeable Batteries with Smart Self-Conditioned Charge and Discharge. *Angew. Chem., Int. Ed.* **2019**, *58*, 9248−9253.
(46) Fang, Z.; Li, Y.; Li, J.; Shu, C.; Zhong, L.; Lu, S.; Mo, C.; Yang, M.; Yu, D. Capturing Visible Light in Low-Band-Gap C_4N-Derived Responsive Bifunctional Air Electrodes for Solar Energy Conversion and Storage. *Angew. Chem., Int. Ed.* **2021**, *60*, 17615−17621.
(47) Tomon, C.; Sarawutanukul, S.; Duangdangchote, S.; Krittayavathananon, A.; Sawangphruk, M. Photoactive Zn-Air Batteries Using Spinel-Type Cobalt Oxide as a Bifunctional Photocatalyst at the Air Cathode. *Chem. Commun.* **2019**, *55*, 5855−5858.
(48) Lv, J.; Abbas, S. C.; Huang, Y.; Liu, Q.; Wu, M.; Wang, Y.; Dai, L. A Photo-Responsive Bifunctional Electrocatalyst for Oxygen Reduction and Evolution Reactions. *Nano Energy* **2018**, *43*, 130−137.
(49) Qiao, G.; Guan, D.; Yuan, S.; Rao, H.; Chen, X.; Wang, J.; Qin, J.; Xu, J.; Yu, J. Perovskite Quantum Dots Encapsulated in a Mesoporous Metal-Organic Framework as Synergistic Photocathode Materials. *J. Am. Chem. Soc.* **2021**, *143*, 14253−14260.
(50) Zhu, Z.; Lv, Q.; Ni, Y.; Gao, S.; Geng, J.; Liang, J.; Li, F. Internal Electric Field and Interfacial Bonding Engineered Step-Scheme Junction for a Visible-Light-Involved Lithium-Oxygen Battery. *Angew. Chem., Int. Ed.* **2022**, *61*, No. e202116699.
(51) Bagwe, R. P.; Yang, C.; Hilliard, L. R.; Tan, W. Optimization of Dye-Doped Silica Nanoparticles Prepared Using a Reverse Micro Emulsion Method. *Langmuir* **2004**, *20*, 8336−8342.
(52) Kim, S.; Moon, G.; Kim, G.; Kang, U.; Park, H.; Choi, W. TiO_2 Complexed with Dopamine-Derived Polymers and the Visible Light Photocatalytic Activities for Water Pollutants. *J. Catal.* **2017**, *346*, 92−100.
(53) Meng, A.; Cheng, B.; Tan, H.; Fan, J.; Su, C.; Yu, J. TiO_2/Polydopamine S-Scheme Heterojunction Photocatalyst with Enhanced CO_2 Reduction Selectivity. *Appl. Catal. B Environ.* **2021**, *289*, 120039.
(54) Dai, K.; Lv, J.; Zhang, J.; Zhu, G.; Geng, L.; Liang, C. Efficient Visible-Light-Driven Splitting of Water into Hydrogen over Surface-Fluorinated Anatase TiO_2 Nanosheets with Exposed {001} Facets/Layered CdS-Diethylenetriamine Nanobelts. *ACS Sustainable Chem. Eng.* **2018**, *6*, 12817−12826.
(55) Li, X.; Xiong, J.; Xu, Y.; Feng, Z.; Huang, J. Defect-Assisted Surface Modification Enhances the Visible Light Photocatalytic Performance of g-C_3N_4@C-TiO_2 Direct Z-Scheme Heterojunctions. *Chin. J. Catal.* **2019**, *40*, 424−433.
(56) He, F.; Zhu, B.; Cheng, B.; Yu, J.; Ho, W.; Macyk, W. 2D/2D/0D $TiO_2/C_3N_4/Ti_3C_2$ MXene Composite S-Scheme Photocatalyst with Enhanced CO_2 Reduction Activity. *Appl. Catal. B Environ.* **2020**, *272*, 119006.
(57) Wang, L.; Tan, H.; Zhang, L.; Cheng, B.; Yu, J. *In-situ* Growth of Few-Layer Graphene on ZnO with Intimate Interfacial Contact for Enhanced Photocatalytic CO_2 Reduction Activity. *Chem. Eng. J.* **2021**, *411*, 128501.
(58) He, T.; Wang, L.; Fabregat-Santiago, F.; Liu, G.; Li, Y.; Wang, C.; Guan, R. Electron Trapping Induced Electrostatic Adsorption of Cations: A General Factor Leading to Photoactivity Decay of Nanostructured TiO_2. *J. Mater. Chem. A* **2017**, *5*, 6455.
(59) He, Z.; Han, Y.; Liu, S.; Cui, W.; Qiao, Y.; He, T.; Wang, Q. Toward the Intrinsic a Superiority of a Ligned One-Dimensional TiO_2 Nanostructures: The Role of Defect States in Electron Transport Process. *ChemElectroChem* **2020**, *7*, 4390−4397.
(60) Ke, X.; Zhang, J.; Dai, K.; Fan, K.; Liang, C. Integrated S-Scheme Heterojunction of Amine-Functionalized 1D CdSe Nanorods Anchoring on Ultrathin 2D $SnNb_2O_6$ Nanosheets for Robust Solar-Driven CO_2 Conversion. *Sol. RRL* **2021**, *5*, 2000805.

https://doi.org/10.1021/acsami.2c19598
ACS Appl. Mater. Interfaces 2023, 15, 6788−6796

Supporting Information

Photo Energy Enhanced Oxygen Reduction and Evolution Kinetics in Zn-Air Batteries

Hange Feng,[a, c] Chaomin Zhang,[b] Menghao Luo,[c] Yuechuan Hu,[c] Zibo Dong,[c] Shaolin Xue[c, d*] and Paul K. Chu[e]

[a] College of Information Science and Technology, Donghua University, Shanghai 201620, P. R. China

[b] School of Mathematics, Physics and Statistics, Shanghai University of Engineering Science, Shanghai 201620, China

[c] College of Science, Donghua University, Shanghai 201620, P. R. China

[d] Shanghai Institute of Intelligent Electronics and Systems, Donghua University, Shanghai 201620, China

[e] Department of Physics, Department of Materials Science and Engineering, and Department of Biomedical Engineering, City University of Hong Kong, Tat Chee Avenue, Kowloon, Hong Kong, China

E-mail addresses: 17721486315@163.com (H. Feng); zhangchaomin@sues.edu.cn (C. Zhang); 2202248@mail.dhu.edu.cn (M. Luo); hyc270322@163.com (Y. Hu); dzb_dhu@163.com (Z. Dong); slxue@dhu.edu.cn (S. Xue); paul.chu@cityu.edu.hk (Paul K. Chu)

* Corresponding author: Fax: +86 21 67792089; E-mail address: slxue@dhu.edu.cn (S.L. Xue)

Materials characterization

The morphology of TiO_2-In_2Se_3 was observed by field-emission scanning electron microscopy (FE-SEM, Hitachi S-4800) and field-emission transmission electron microscopy (FE-TEM, JEOL JEM-2100F). X-ray diffraction (XRD) was conducted on the Rigaku MiniFlex600 with Cu K_α radiation (λ = 1.5406 Å) and X-ray photoelectron spectroscopy (XPS) was carried out on the Perkin Elmer PHI1600 ESCA. The nitrogen adsorption/desorption isotherms were obtained using a nitrogen adsorber (Micromeritics TriStarII 3020, USA) to determine the specific surface area of the samples. Photoluminescence was performed on the Edinburgh FLS 920 and the optical absorbance was measured by UV-Vis spectrophotometry (UV-vis; G-9, Rangqi, China). The specific surface area and pore volume of TiO_2-In_2Se_3 were determined by Quadrasorbevo 2QDS-MP-30. The hydroxyl and superoxide radicals generated in the reactions were analyzed by electron paramagnetic resonance (EPR) using 5, 5-dimethyl-L-pyrroline N-oxide (DMPO) as the trap for the reactive species (EMX Nano, Bruke).

Electrochemical characterization

The electrochemical experiments were carried out on the CHI760E electrochemical workstation and the ORR and OER characteristics of TiO_2-In_2Se_3 were evaluated by linear voltammetry (LSV) based on the three-electrode configuration with TiO_2-In_2Se_3 being the working electrode, Hg/HgO as the reference electrode, and graphite rod as the counter electrode in the O_2-saturated 0.1 M KOH electrolyte. The surface of the electrode was illuminated by an ultraviolet light source (power of 90 mW cm^{-2} and wavelength of 365 nm). Electrochemical impedance spectroscopy (EIS) was conducted at an AC voltage of 10 mV int the frequency range between 0.01 Hz and 100 kHz. The reference experiments were performed under the same conditions and the reference catalyst was Pt/C.

Calculation of incident photon-to-current efficiency (IPCE): The IPCE of TiO_2-In_2Se_3 is calculated by the following equation:

$$\text{IPCE (\%)} = |E_L - E_D| \times I/P_{in} \times 100\%$$

E_L and E_D represent the discharge/charge voltage of the ZABs with and without illumination, respectively. I is the current density and P_{in} is the illumination power of 90 mW cm^{-2}.

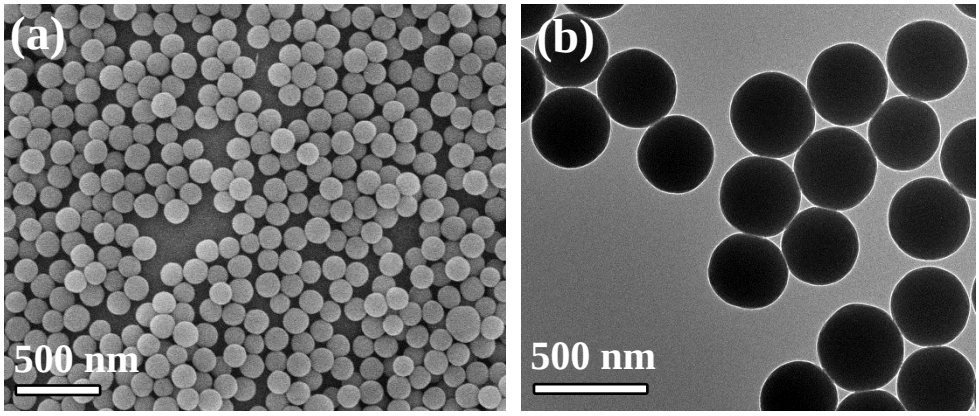

Figure S1. (a) SEM image and (b) TEM image of SiO_2.

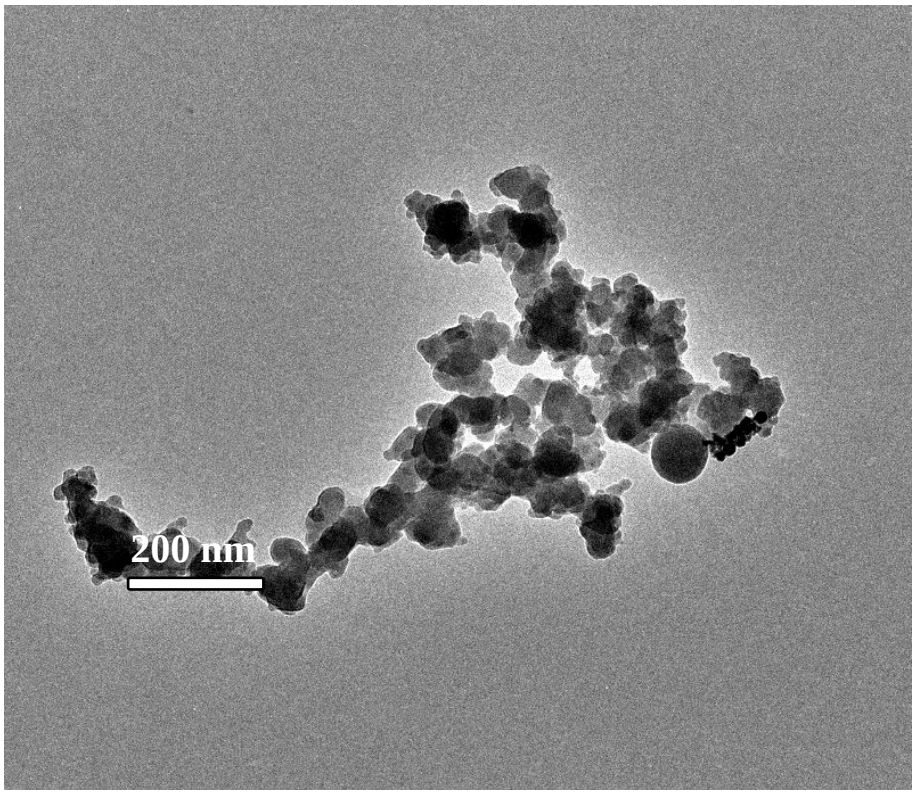

Figure S2. TEM image of In_2Se_3.

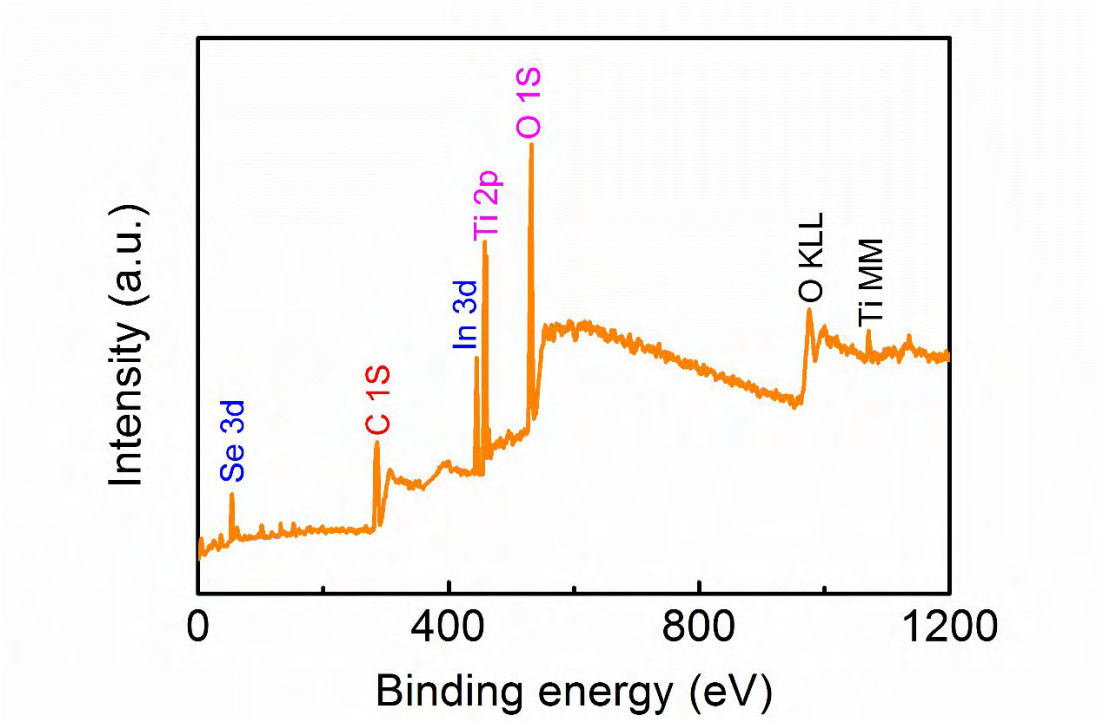

Figure S3. XPS survey spectrum of TiO_2-In_2Se_3.

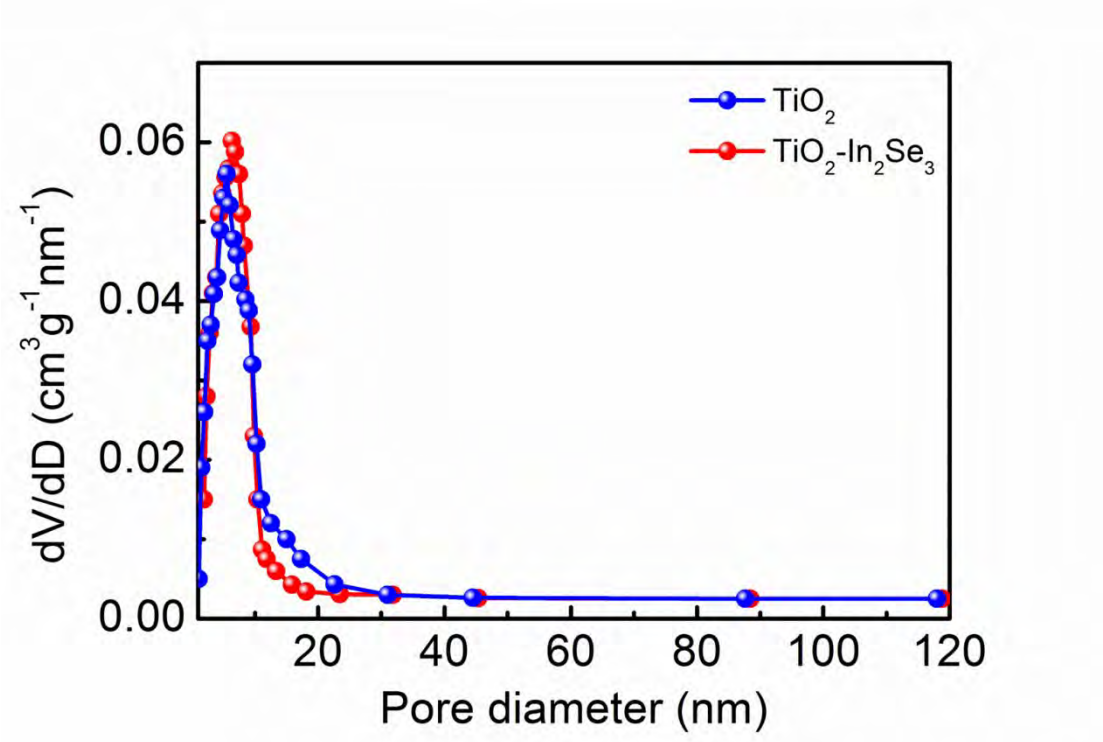

Figure S4. Pore size distributions of TiO_2, TiO_2-In_2Se_3.

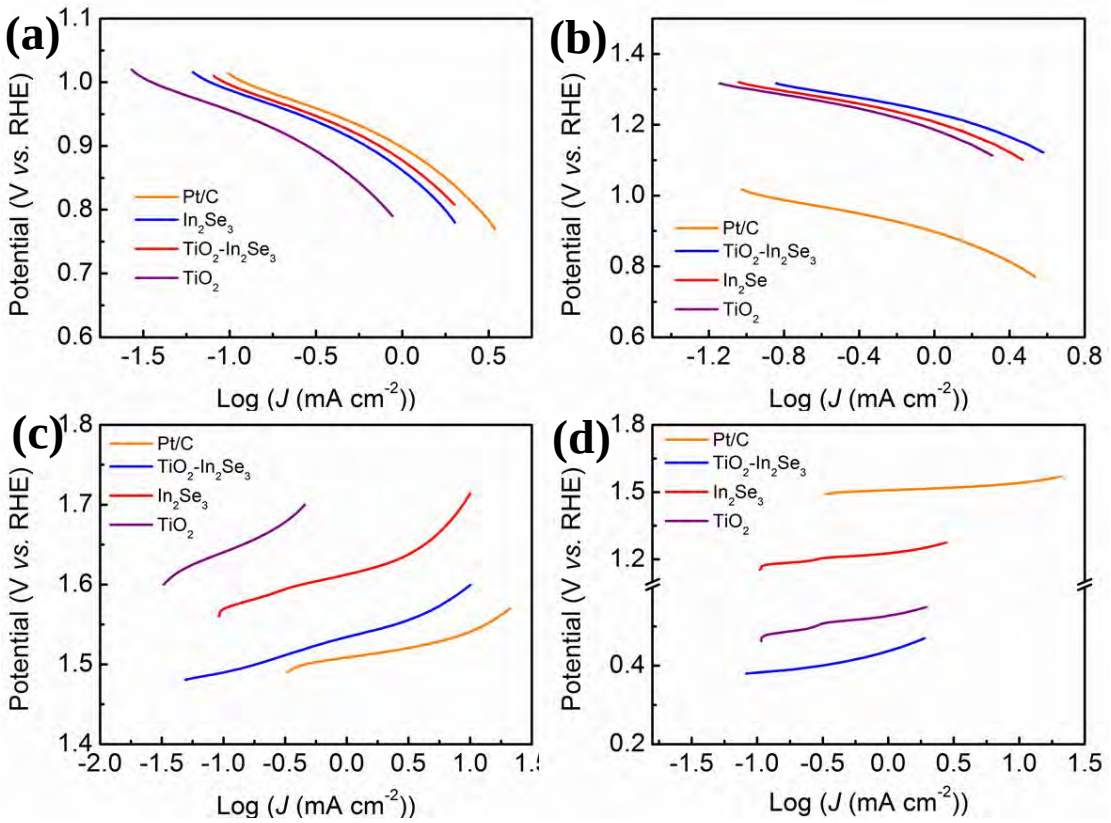

Figure S5. ORR Tafel plots of Pt/C, TiO_2, In_2Se_3 and TiO_2-In_2Se_3: (a) Without light illumination and (b) Under light illumination; OER Tafel plots of Pt/C, TiO_2, In_2Se_3 and TiO_2-In_2Se_3: (c) Withoug light illumination and (d) Under light illumination.

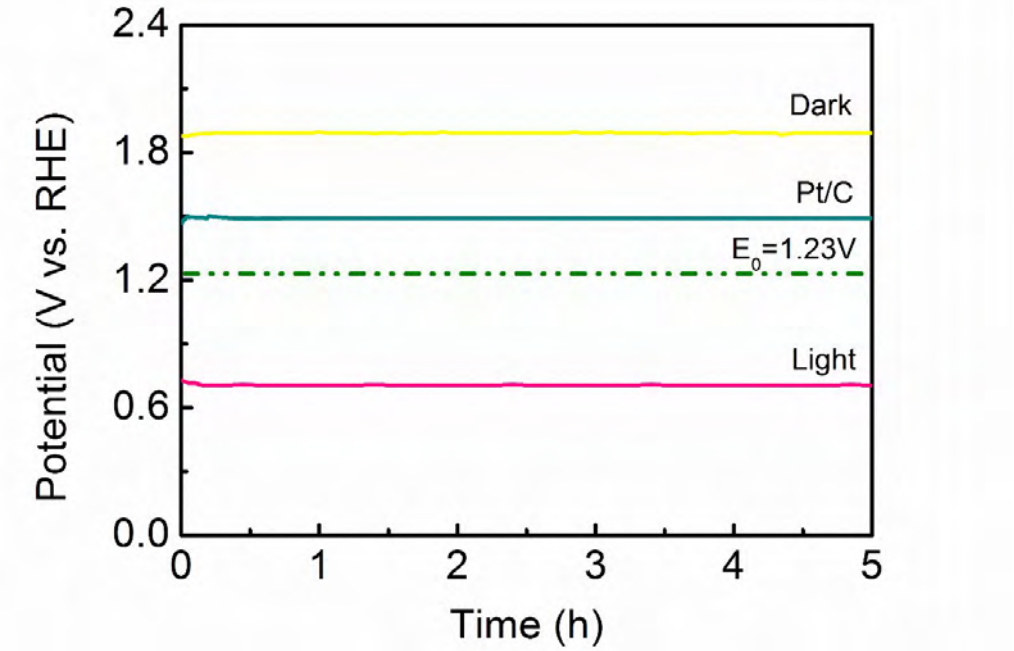

Figure S6. Polarization curves of TiO_2-In_2Se_3 with and without light irradiation in comparison with Pt/C.

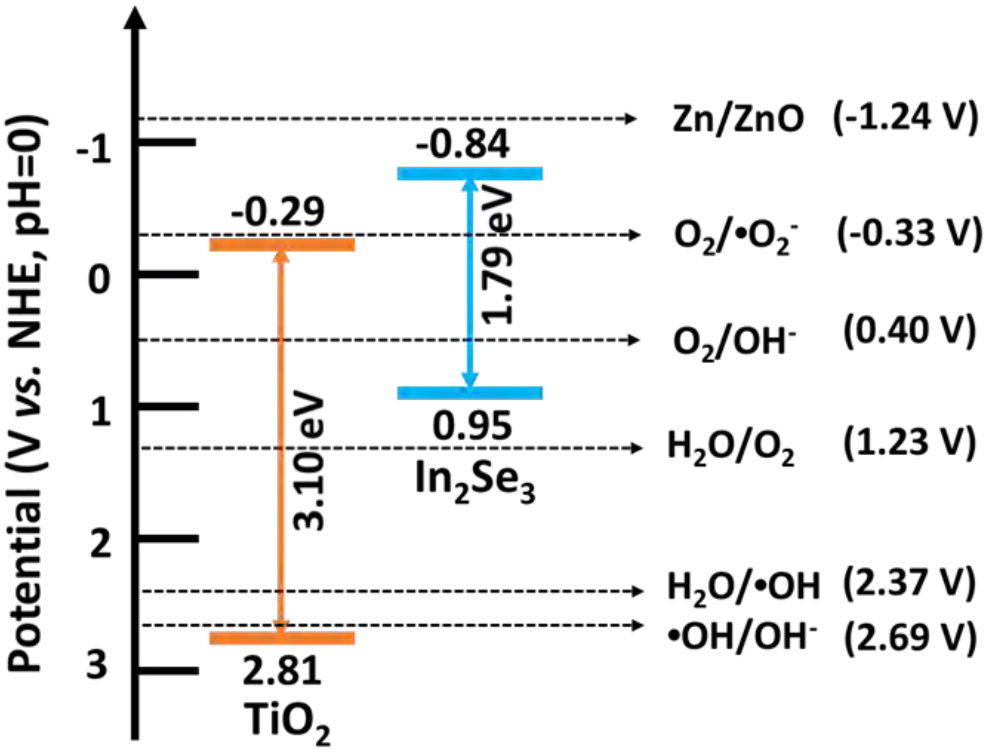

Figure S7. Band structures of TiO_2 and In_2Se_3.

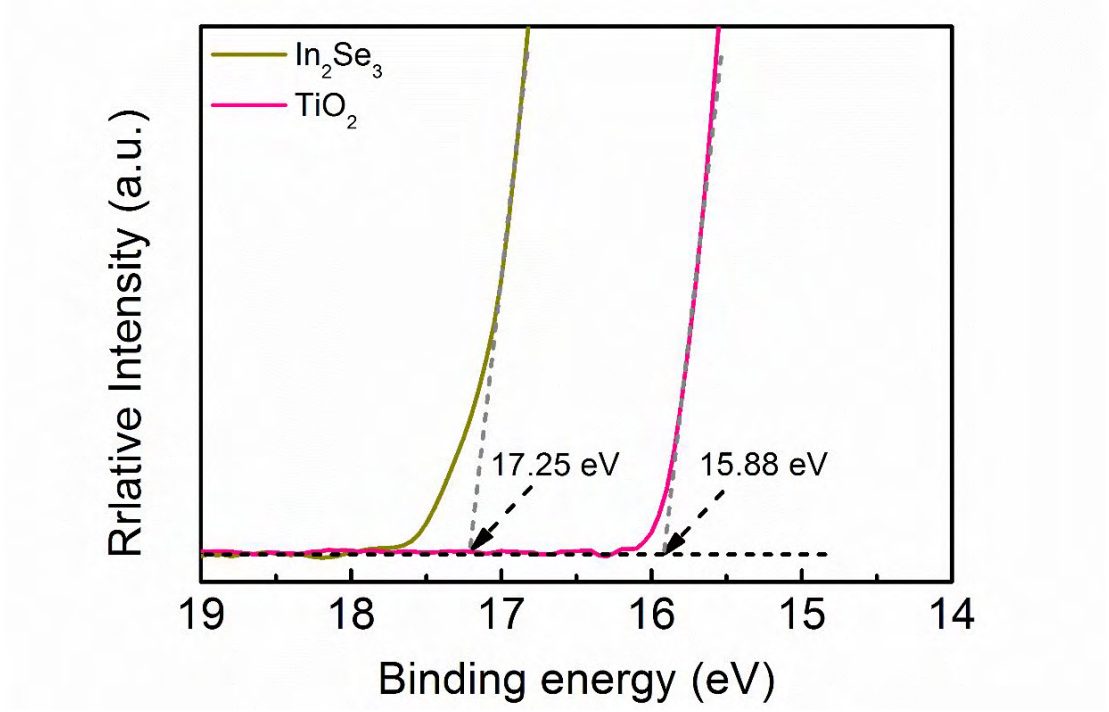

Figure S8. UPS plots of TiO_2 and In_2Se_3.

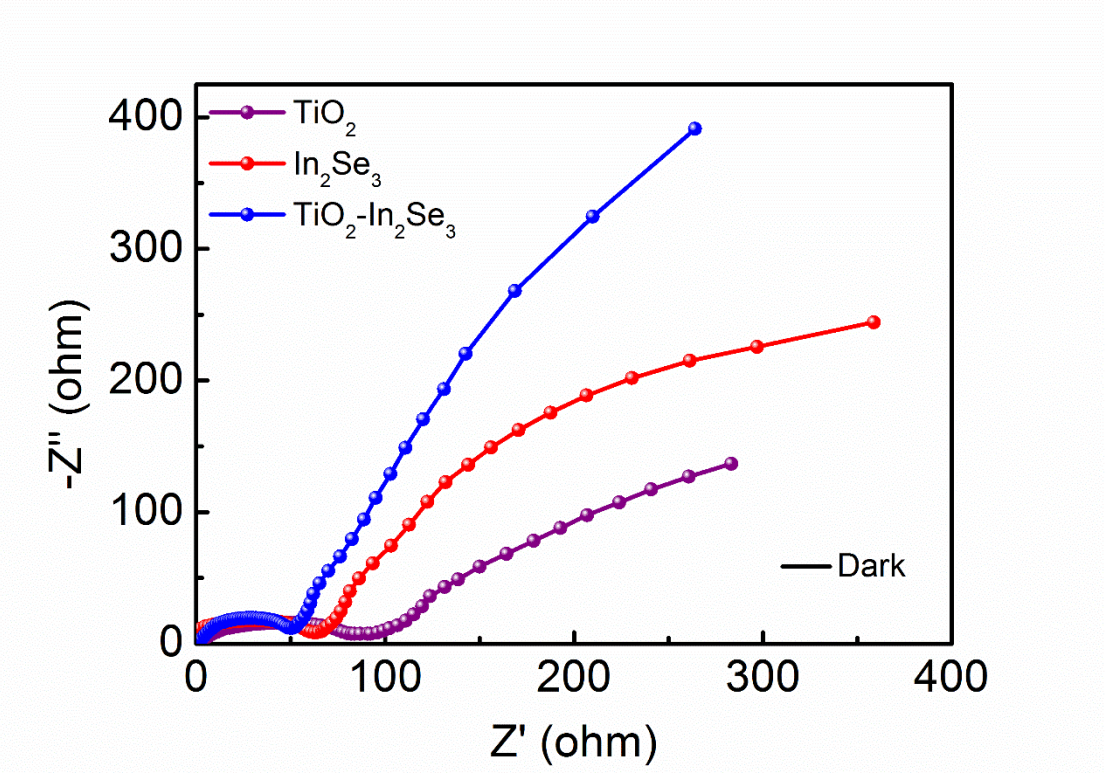

Figure S9. EIS curves of TiO_2, In_2Se, and TiO_2-In_2Se_3 without light illumination.

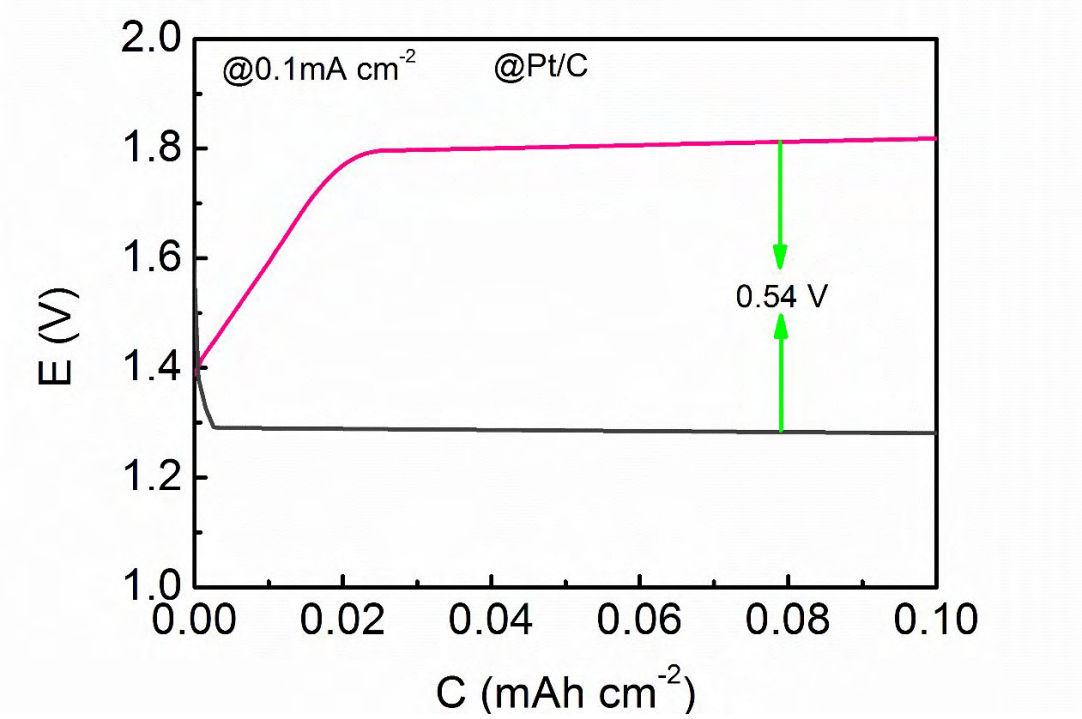

Figure S10. Discharging and charging curves of Pt/C at 0.1 mA cm^{-2}.

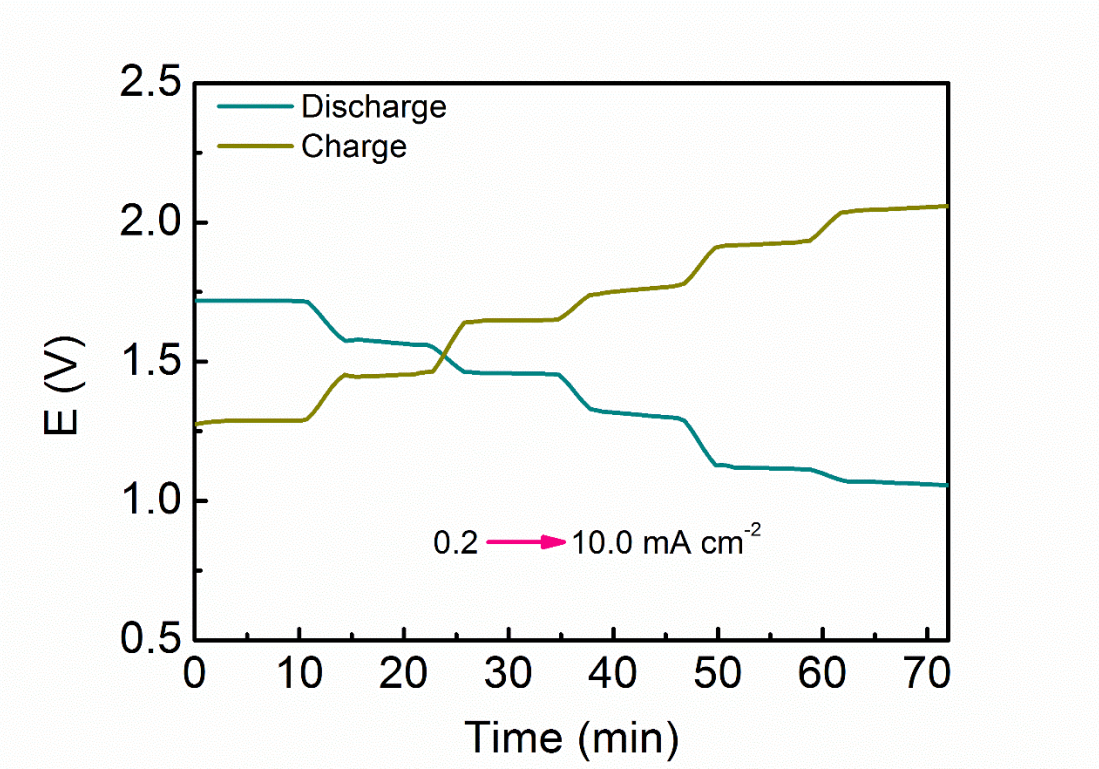

Figure S11. Discharging/charging curves of TiO_2-In_2Se_3 at different current densities of 0.2, 0.5, 1.0, 2.0, 5.0, and 10.0 mA cm^{-2} with and without AM 1.5 illumination.

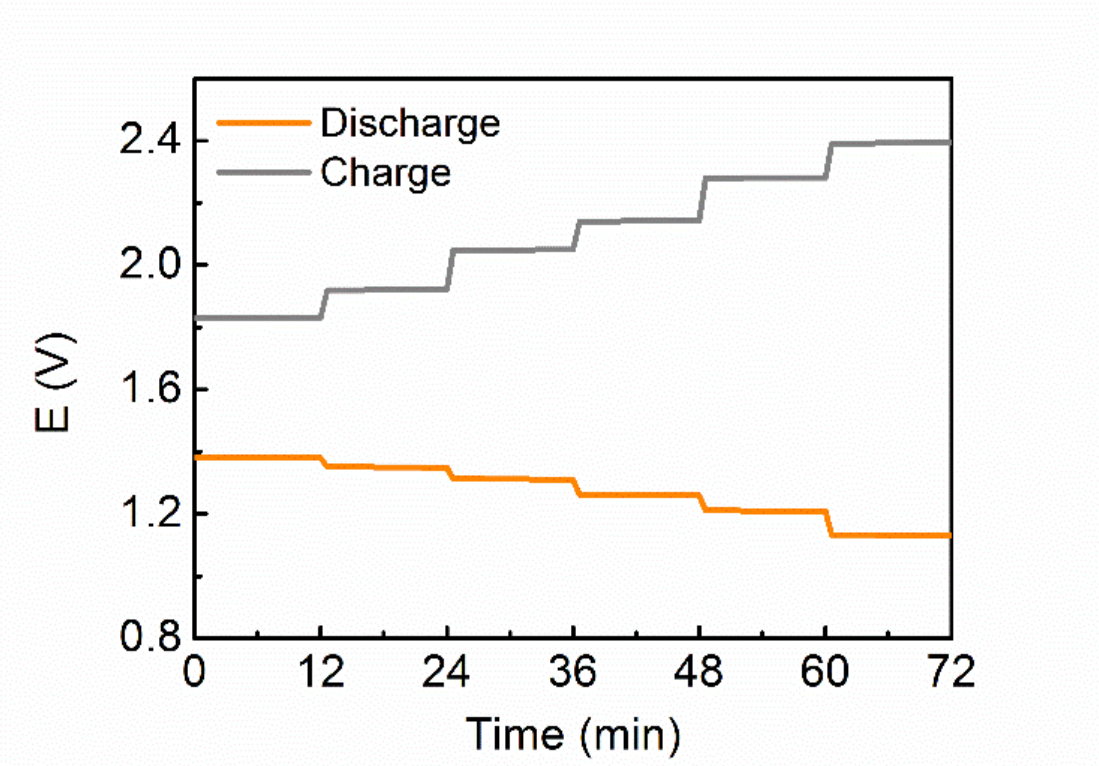

Figure S12. Discharge/charge curves of ZAB at 0.2, 0.5, 1.0, 2.0, 5.0 and 10.0 mA cm^{-2}.

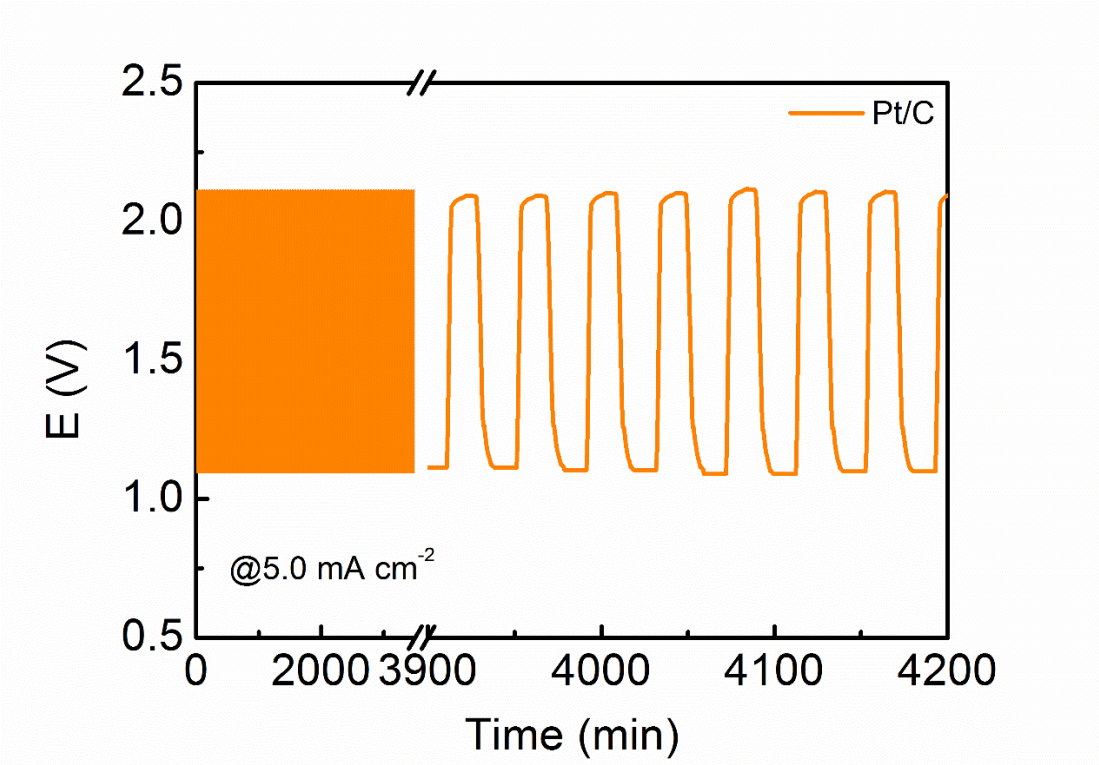

Figure S13. Cycling characteristics of Pt/C at 5.0 mA cm^{-2}.

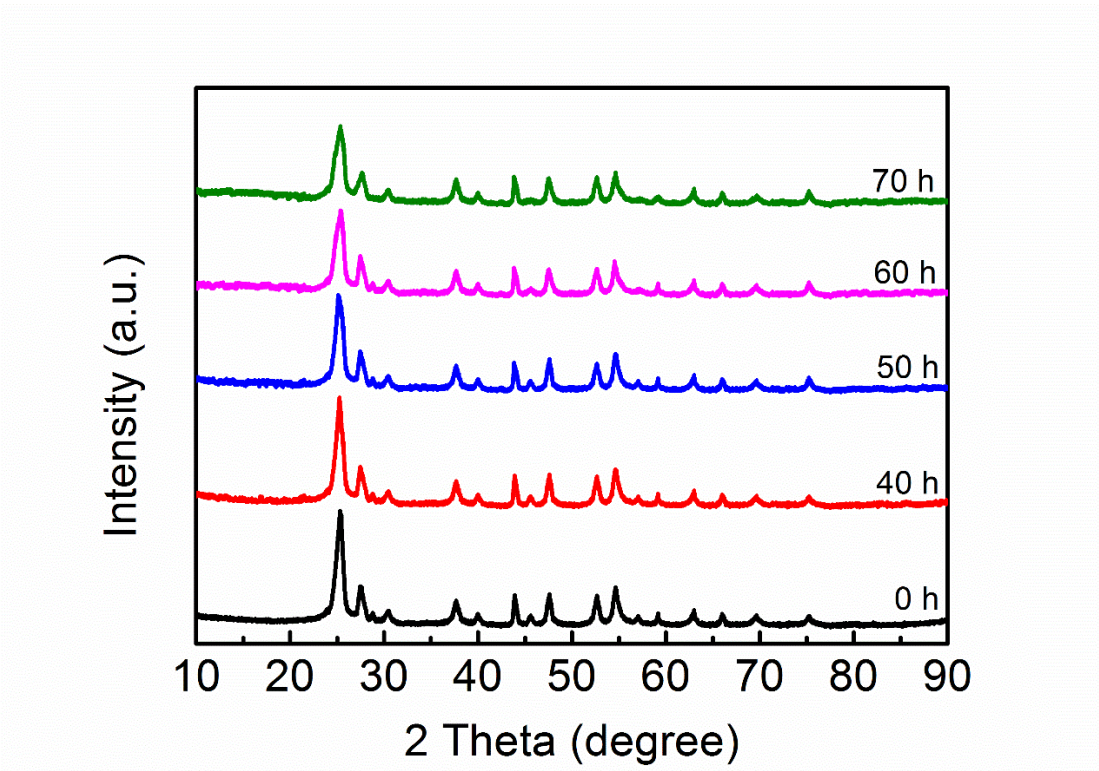

Figure S14. XRD spectra of TiO_2-In_2Se_3 after testing at 5.0 mA cm^{-2} for 70 h.

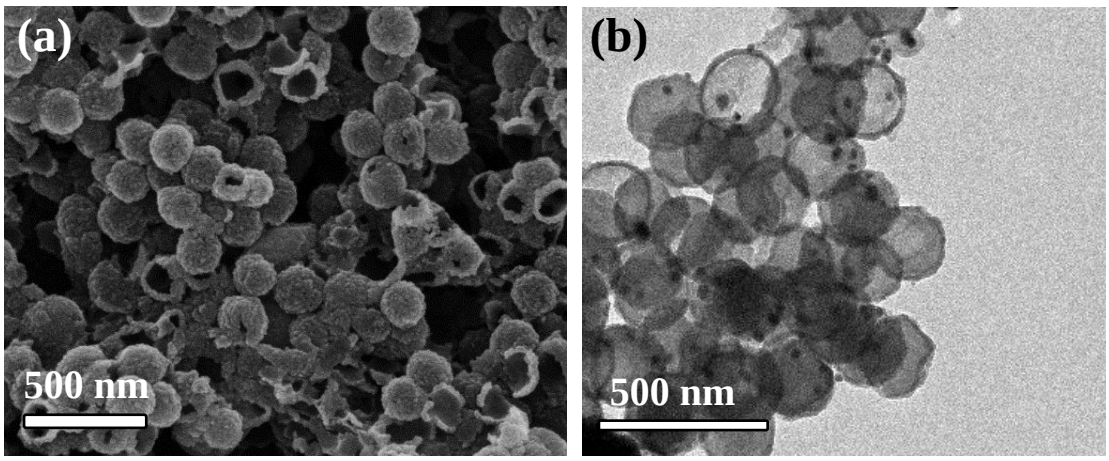

Figure S15. SEM and TEM images of TiO_2-In_2Se_3 after testing at 5.0 mA cm^{-2} for 70h.

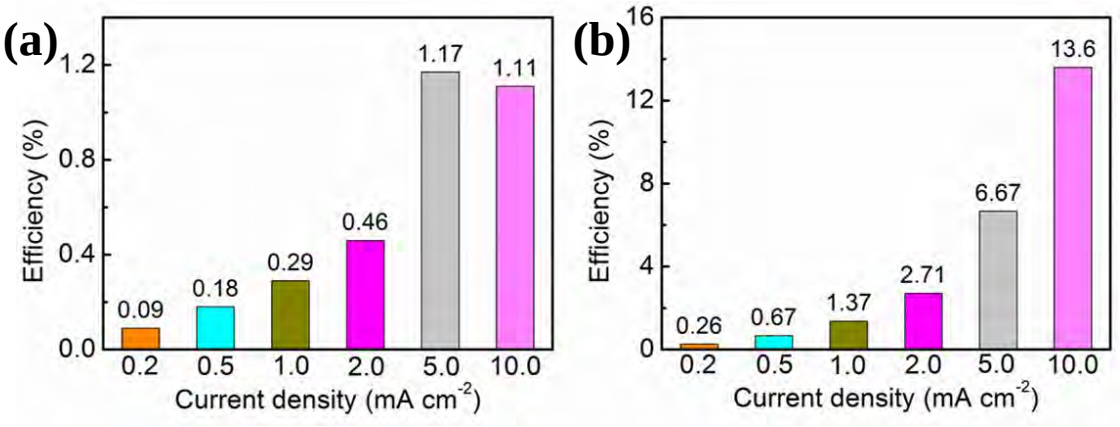

Figure S16. The incident photon-current efficiency (IPCE) of ZABs in (a) discharging and (b) charging process at different current densities under 90 mW cm^{-2}.

Table S1. Charge carrier lifetime derived from time-resolved PL decay.

Samples	A_1 (%)	τ_1	A_2 (%)	τ_2	τ_a
TiO_2	57.62	1.49	42.38	4.98	3.97
In_2Se_3	63.19	1.36	36.81	4.82	3.69
TiO_2-In_2Se_3	36.43	1.08	63.57	3.26	2.91

Table S2. Comparison of the battery properties of the materials described in this paper with those of recently reported Zn-air batteries with and without light illumination.

	Cathodes	Charging Voltages	Discharging Voltages	Current Densities	References
Light-irradiated Zn-air Batteries	TiO_2-In_2Se_3	0.67 V	1.79 V	0.1 mA cm^{-2}	This work
		1.12 V	1.39 V	5.0 mA cm^{-2}	
	pTTh	0.78 V	1.98 V	0.1 mA cm^{-2}	1
	PEDOT-PEO-CNTs-PUF	1.88 V	1.0 V	1.0 mA cm^{-2}	2
	α-Fe_2O_3	1.64 V	1.15 V	0.5 mA cm^{-2}	3
	$BiVO_4$	1.46 V	1.30 V	0.5 mA cm^{-2}	
State-of the-art Zn-air Batteries	Mn/Fe-HIB-MOF	1.85 V	1.21 V	10.0 mA cm^{-2}	4
	Co_3O_4/N-CNT	2.0 V	1.0 V	2.0 mA cm^{-2}	5
	Co_9S_8-NSHPCNF	2.0 V	1.16 V	10.0 mA cm^{-2}	6
	Ce doped $LaCoO_3$	1.80 V	1.17 V	2.0 mA cm^{-2}	7

References

[1] Zhu, D.; Zhao, Q.; Fan, G.; Zhao, S.; Wang, L.; Li, F.; Chen, J. Photoinduced Oxygen Reduction Reaction Boosts the Output Voltage of a Zinc-Air Battery. *Angew. Chem. Int. Ed.* **2019**, *58*, 12460.

[2] Fang, Z.; Zhang, Y.; Hu, X.; Fu, X.; Dai, L.; Yu, D. Tactile UV-and Solar-Light Multi-Sensing Rechargeable Batteries with Smart Self-Conditioned Charge and Discharge. *Angew. Chem. Int. Ed.* 2019, *58*, 9248-9253.

[3] Liu, X.; Yuan, Y.; Liu, J.; Liu, B.; Chen, X.; Ding, J.; Han, X.; Deng, Y.; Zhong, C.; Hu, W. Utilizing Solar Energy to Improve the Oxygen Evolution Reaction Kinetics in Zinc-Air Battery. *Nat. Commun.* **2019**, *10*, 1-10.

[4] Shinde, S.; Lee, C.; Jung, J.; Wagh, N.; Kim, S.; Kim, D.; Lin, C.; Lee, S.; Lee, J. Unveiling Dual-Linkage 3D Hexaiminobenzene Metal-Organic Frameworks towards Long-Lasting Advanced Reversible Zn-Air Batteries. *Energy Environ. Sci.* **2019**, *12*, 727-738.

[5] Zeng, S.; Chen, H.; Wang, H.; Tong, X.; Chen, M.; Di, J.; Li, Q. Crosslinked Carbon Nanotube Aerogel Films Decorated with Cobalt Oxides for Flexible Rechargeable Zn-Air Batteries. *Small* **2017**, *13*, 1700518.

[6] Peng, W.; Wang, Y.; Yang, X.; Mao, L.; Jin, J.; Yang, S.; Fu, K.; Li, G. Co_9S_8 Nanoparticles Embedded in Multiple Doped and Electrospun Hollow Carbon Nanofibers as Bifunctional Oxygen Electrocatalysts for Rechargeable Zinc-Air Battery, *Appl. Catal. B: Environ.* **2020**, *268*, 118437.

[7] Qian, J.; Wang, T.; Zhang, Z.; Liu, Y.; Li, J.; Gao, D. Engineered Spin State in Ce Doped $LaCoO_3$ with Enhanced Electrocatalytic Activity for Rechargeable Zn-Air Batteries, *Nano Energy* **2020**, *74*, 104948.